

Flavor origin of dark matter and its relation with leptonic nonzero θ_{13} and Dirac CP phase δ

Subhaditya Bhattacharya^a Biswajit Karmakar,^a Narendra Sahu^b Arunansu Sil^a

^a*Department of Physics, Indian Institute of Technology Guwahati, 781039 Assam, India*

^b*Department of Physics, Indian Institute of Technology, Hyderabad, Kandi, Sangareddy 502285, Medak, Telengana, India*

E-mail: subhab@iitg.ernet.in, k.biswajit@iitg.ernet.in,
nsahu@iith.ac.in, asil@iitg.ernet.in

ABSTRACT: We propose a minimal extension of the standard model by including a $U(1)$ flavor symmetry to establish a correlation between the relic abundance of dark matter, measured by WMAP and PLANCK satellite experiments and non-zero value of $\sin\theta_{13}$ observed at DOUBLE CHOOZ, Daya Bay, RENO and T2K. The flavour symmetry is allowed to be broken at a high scale to a remnant \mathcal{Z}_2 symmetry, which not only ensures the stability to the dark matter, but also gives rise to a modification to the existing A_4 -based tri-bimaximal neutrino mixing. This deviation in turn suggests the required non-zero value of $\sin\theta_{13}$. We assume the dark matter to be neutral under the existing A_4 symmetry while charged under the $U(1)$ flavor symmetry. Hence in this set-up, the non-zero value of $\sin\theta_{13}$ predicts the dark matter charge under $U(1)$, which can be tested at various ongoing and future direct and collider dark matter search experiments. We also point out the involvement of nonzero leptonic CP phase δ , which plays an important role in the analysis.

ARXIV EPRINT: [1611.07419](https://arxiv.org/abs/1611.07419)

Contents

1	Introduction	1
2	Structure of the model	3
2.1	Neutrino Sector	3
2.2	Dark sector and its interaction with neutrino sector	5
3	Phenomenology of the neutrino sector	6
3.1	Case A : $\phi_{ab} = \phi_{db} = 0$	8
3.2	Case B : $\phi_{db} = 0$	11
3.3	Case C : $\phi_{ab} = 0$	13
3.4	Case D : $\phi_{ab} = \phi_{db} = \beta$	14
4	Phenomenology of DM Sector	16
5	Correlation between Dark and Neutrino Sectors	29
6	Conclusions	31

1 Introduction

After the Higgs discovery at the LHC, the standard model (SM) of particle physics seems to be complete. However, it does not explain many current issues in particle physics which are supported by experiments. In particular, the oscillation experiments [1–4] confirm that the neutrinos are massive and they mix with each other. Contrary to this finding, neutrinos are massless within the framework of SM. Another outstanding problem in particle physics as of today is the nature of dark matter (DM), whose relic abundance is precisely measured by the WMAP [5] and PLANCK [6] satellite experiments to be $0.094 \leq \Omega_{\text{DM}} h^2 \leq 0.130$. In fact, the existence of DM is strongly supported by the galactic rotation curve, gravitational lensing and large scale structure of the Universe [8] as well. However, the SM of particle physics fails to provide a candidate of DM. In this work our aim is to go beyond the SM of particle physics to explore scenarios which can accommodate a candidate of DM as well as non-zero neutrino masses and mixings.

Flavor symmetries are often used to explore many unsolved issues within and beyond the SM of particle physics. For example, a global $U(1)$ flavor symmetry was proposed a long ago to explain the quark mass hierarchy and Cabibbo mixing angle [9]. Subsequently many flavor symmetric frameworks have been adopted to explain neutrino masses and mixings in the lepton sector. In particular, a tri-bimaximal (TBM) lepton mixing generated from a discrete flavor symmetry such as A_4 attracts a lot of attention [10, 11] due to its simplicity and predictive nature. However the main drawback of these analyses was that it

predicts vanishing reactor mixing angle θ_{13} which is against the recent robust observation of $\theta_{13} \approx 9^\circ$ [12–14] by DOUBLE CHOOZ [15], Daya Bay [16], RENO [17] and T2K [18] experiments. Hence, a modification of the TBM structure of lepton mixing is required.

In this work we consider the existence of a dark sector [19] consisting of vector-like fermions which are charged under an additional $U(1)$ flavor symmetry. Specifically, we consider a vector-like SM singlet fermion (χ^0) and a $SU(2)_L$ doublet fermion (ψ) which are odd under the remnant \mathcal{Z}_2 symmetry generated from the broken $U(1)$. The neutral components mix to give rise a fermionic DM (ψ_1). Note that in the simplest case, a singlet fermion (χ^0) can generate a Higgs portal interaction by dimension five operator suppressed by the new physics scale as $(\overline{\chi^0}\chi^0 H^\dagger H)/\Lambda$. However, as we argue, that the new physics scale (Λ) involved in the theory has to generate the required neutrino mass as well and thus making it very high. As a result, the annihilation rate of DM becomes too small which in turn make the relic density over abundant. On the other hand, a vector-like fermion doublet (ψ) suffers from a large annihilation cross-section to SM through Z mediation and is never enough to produce the required density. It is only through the mixing of these two that can produce correct relic density as we demonstrate here. We also assume the existence of a TBM neutrino mixing pattern (in a basis where charged leptons are diagonal) based on A_4 symmetry. The interaction between the dark and the lepton sector of the SM is mediated by flavon fields charged under the $U(1)$ and/or A_4 . These flavons also take part in producing additional interactions involving lepton and Higgs doublets. The $U(1)$ symmetry, once allowed to be broken by the vacuum expectation value (vev) of a flavon, generates a non-zero $\sin\theta_{13}$ after the electroweak symmetry breaking (and when A_4 breaks too). We show that the non-zero value of $\sin\theta_{13}$ is proportional to the strength of Higgs portal coupling of DM giving rise to the correct relic density. In other words, the precise value of $\sin\theta_{13}$ and DM relic density can fix the charge of dark matter under $U(1)$ flavor symmetry. Indeed it is true for the Dirac CP violating phase $\delta = 0$ as shown in our previous work [20]. However, we have found here that the non-zero values of δ plays an important role for the determination of DM charge under $U(1)$ flavor symmetry. Although the current allowed range of δ ($0^\circ - 360^\circ$) can significantly increase the uncertainty in the determination of DM flavor charge (compared to $\delta = 0$ scenario), a future measurement of δ would be important in fixing the charge. In [20], we have assumed a prevailing TBM pattern and here in this work we provide an explicit construction of that too. We also show that the effective Higgs portal coupling of the vector-like leptonic DM can be tested at future direct search experiments, such as Xenon1T [21] and at the Large Hadron Collider (LHC) [19, 22, 23].

The draft is arranged as follows. In section 2 we discuss the relevant model for correlating non-zero $\sin\theta_{13}$ to Higgs portal coupling of DM which gives correct relic density. In section 3 and 4, we obtain the constraints on model parameters from neutrino masses and mixing and relic abundance of dark matter respectively. In section 5, we obtain the correlation between the non-zero $\sin\theta_{13}$ and Higgs portal coupling of dark matter and conclude in section 6.

2 Structure of the model

In this section, we describe the field content and symmetries involved. We consider an effective field theory approach for realizing the neutrino masses and mixing while trying to connect it with the DM sector as well. The set-up includes the interaction between these two sectors which has the potential to generate adequate θ_{13} , and hence a deviation of TBM mixing happens, to match with the experimental observation while satisfying the constraints from relic density and direct search of DM.

2.1 Neutrino Sector

Field	e_R	μ_R	τ_R	ℓ	H	ψ	χ^o	ϕ_S	ϕ_T	ξ	η	ϕ
$SU(2)_L$	1	1	1	2	2	2	1	1	1	1	1	1
A_4	1	$1''$	$1'$	3	1	1	1	3	3	1	$1'$	1
Z_3	ω	ω	ω	ω	1	1	1	ω	1	ω	ω	1
Z_2	-1	-1	-1	1	1	-1	-1	1	-1	1	1	1
$U(1)$	0	0	0	0	0	q_1	q_2	0	0	0	$-x$	x

Table 1. Fields content and transformation properties under the symmetries imposed on the model. Here $nx = q_1 - q_2$ (justified from Eq.(2.8)), n will be determined later.

The basic set-up relies on the A_4 symmetric construction of the Lagrangian associated with neutrino mass term [10, 11]. Based on the construction by Altarelli-Feruglio (AF) model [11] (for generating TBM mixing), we have extended the flavon sector and symmetry of the model. The SM doublet leptons (ℓ) transform as triplet under the A_4 symmetry while the singlet charged leptons: e_R, μ_R and τ_R transform as $1, 1''$ and $1'$ respectively under A_4 . The flavon fields and their charges (along with the SM fields) are described in Table 1. The flavons ϕ_S, ϕ_T and ξ break the A_4 flavor symmetry by acquiring vevs in suitable directions. Note that here ϕ_S and ϕ_T transform as A_4 triplets but the flavon ξ and the SM Higgs doublet (H) transform as a singlet under A_4 . So the contribution to the effective neutrino mass matrix coming through the higher dimensional operator respecting the symmetries considered can be written as

$$-\mathcal{L}_{\nu_0} = (\ell H \ell H)(y_1 \xi - y_2 \phi_S)/\Lambda^2, \quad (2.1)$$

where Λ is the cut off scale of the theory and y_1, y_2 represents respective coupling constant. The scalar fields break the flavor symmetry when acquire vevs along¹ $\langle \phi_S \rangle = (v_S, 0, 0)$, $\langle \phi_T \rangle = v_T(1, 1, 1)$, $\langle \xi \rangle = v_\xi$ and $\langle H \rangle = v$. As a result we obtain the light neutrino mass matrix as

$$(m_\nu)_0 = \begin{pmatrix} a - 2b/3 & b/3 & b/3 \\ b/3 & -2b/3 & a + b/3 \\ b/3 & a + b/3 & -2b/3 \end{pmatrix}, \quad (2.2)$$

¹The chosen vev alignments of ϕ_S and ϕ_T can be obtained by minimizing the potential involving them along a similar line followed in [11, 24–26].

where $a = y_1(v^2/\Lambda)\epsilon$ and $b = y_2(v^2/\Lambda)\epsilon$, with $\epsilon = v_\xi/\Lambda = v_S/\Lambda$ is considered without loss of generality as any prefactor (due to the mismatch of vevs) can be absorbed in the definition of y_2 . The above mass matrix can be diagonalized by the TBM mixing matrix [27]

$$U_{TB} = \begin{pmatrix} \sqrt{\frac{2}{3}} & \frac{1}{\sqrt{3}} & 0 \\ -\frac{1}{\sqrt{6}} & \frac{1}{\sqrt{3}} & -\frac{1}{\sqrt{2}} \\ -\frac{1}{\sqrt{6}} & \frac{1}{\sqrt{3}} & \frac{1}{\sqrt{2}} \end{pmatrix}. \quad (2.3)$$

The relevant contribution to charged leptons (considering charges from Table 1) can be obtained via

$$\mathcal{L}_l = \frac{y_e}{\Lambda} (\bar{\ell}\phi_T) H e_R + \frac{y_\mu}{\Lambda} (\bar{\ell}\phi_T)' H \mu_R + \frac{y_\tau}{\Lambda} (\bar{\ell}\phi_T)'' H \tau_R, \quad (2.4)$$

which yields the diagonal mass matrix:

$$M_l = \begin{pmatrix} y_e v \frac{v_T}{\Lambda} & 0 & 0 \\ 0 & y_\mu v \frac{v_T}{\Lambda} & 0 \\ 0 & 0 & y_\tau v \frac{v_T}{\Lambda} \end{pmatrix}. \quad (2.5)$$

Note that this is the leading order contribution (and is proportional to $1/\Lambda$) in the charged lepton mass matrix. Due to the symmetry of the model as described in Table 1 (including the $U(1)$ symmetry to be discussed later) there will be no term proportional to $1/\Lambda^2$. Therefore no contribution to the lepton mixing matrix originated from the charged lepton sector up to $1/\Lambda^2$ is present. Here it is worthy to mention that the dimension-5 operator $\ell H \ell H/\Lambda$ is forbidden due to the Z_3 symmetry specified in Table 1. This additional symmetry also forbids the dimension-6 operator $\ell H \ell H (\phi_T + \phi_T^\dagger)/\Lambda^2$. The $U(1)$ flavor symmetry considered here does not allow terms involving ϕ, η (such as: $\ell H \ell H (\phi + \eta)/\Lambda^2$) as discussed (where ϕ and η are charged under $U(1)$ but the SM particles are not). Therefore, Eq. (2.1) is the only relevant term up to $1/\Lambda^2$ order contributing to the neutrino mass matrix $(m_\nu)_0$ ensuring its TBM structure as in Eq. (2.2). Note that these kind of structure of the neutrino mass matrix of $(m_\nu)_0$ can also be obtained in a A_4 based set-up either in a type-I, II or inverse seesaw framework [28–31].

The immediate consequence of TBM mixing as given in Eq. (2.3) is that it implies $\sin^2 \theta_{12} = 1/3$, $\sin^2 \theta_{23} = 1/2$ and $\sin \theta_{13} = 0$. Now to explain the current experimental observation on θ_{13} we consider an operator of order $1/\Lambda^3$:

$$-\delta\mathcal{L}_\nu = y_3 \frac{(\ell H \ell H)\phi\eta}{\Lambda^3}, \quad (2.6)$$

where we have introduced two other SM singlet flavon fields ϕ and η which carry equal and opposite charges under the $U(1)$ symmetry but transform as 1 and $1'$ under A_4 respectively. The $U(1)$ charge assignment to these two flavons also ensures that ϕ and η do not take part in $(m_\nu)_0$. Thus, after flavor and electroweak symmetry breaking this term contributes to the light neutrino mass matrix as follows:

$$\delta m_\nu = \begin{pmatrix} 0 & 0 & d \\ 0 & d & 0 \\ d & 0 & 0 \end{pmatrix}, \quad (2.7)$$

where $d = y_3(v^2/\Lambda)\epsilon^2$ with $\epsilon = \langle\phi\rangle/\Lambda \equiv \langle\eta\rangle/\Lambda$. This typical flavor structure of the additional contribution in the neutrino mass matrix follows from the involvement of η field, which transforms as $1'$ under A_4 [28, 32]. This δm_ν can indeed generate the $\theta_{13} \neq 0$ in the same line as in [28, 30, 31]. Note that the choice of Z_2 symmetry presented in Table 1 also forbids the contributions to neutrino mass matrix proportional to $1/\Lambda^3$ (involving terms like $\ell H \ell H \phi_S \phi_T$, $\ell H \ell H \xi \phi_T$, $\ell H \ell H \phi_S \phi_T^\dagger$ and $\ell H \ell H \xi \phi_T^\dagger$) and thus ensuring Eq. (2.7) is the only contribution responsible for breaking the TBM mixing.

2.2 Dark sector and its interaction with neutrino sector

The dark sector associated with the present construction consists of a vector-like $SU(2)_L$ doublet $\psi^T = (\psi^0, \psi^-)$ and a neutral singlet fermion χ^0 [19], which are odd under the Z_2 symmetry as has already been mentioned in Table 1. These fermions are charged under an additional $U(1)$ flavor symmetry, but neutral under the existing symmetry in the neutrino sector (say the non-Abelian A_4 and additional discrete symmetries required). Note that all the SM fields and the additional flavons in the neutrino sector except ϕ are neutral under this additional $U(1)$ symmetry. Since ψ and χ^0 are vector-like fermions, they can have bare masses, M_ψ and M_χ , which are not protected by the SM symmetry. The effective Lagrangian, invariant under the symmetries considered, describing the interaction between the dark and the SM sector is then given by:

$$\mathcal{L}_{\text{int}} = \left(\frac{\phi}{\Lambda}\right)^n \bar{\psi} \tilde{H} \chi^0, \quad (2.8)$$

where n is not fixed at this stage. The above term is allowed provided the $U(1)$ charge of ϕ^n is compensated by ψ and χ^0 *i.e.* $nx = q_1 - q_2$. We will fix it later from phenomenological point of view.

When ϕ acquires a vev, the $U(1)$ symmetry breaks down and an effective Yukawa interaction is generated between the SM and the DM sectors. After electroweak symmetry is broken, the DM emerges as an admixture of the neutral component of the vector-like fermions ψ , *i.e.* ψ^0 , and χ^0 . The Lagrangian describing the DM sector and the interaction as a whole reads as

$$-\mathcal{L}_{\text{Yuk}} \supset M_\psi \bar{\psi} \psi + M_\chi \bar{\chi}^0 \chi^0 + \left[Y \bar{\psi} \tilde{H} \chi^0 + \text{h.c.} \right], \quad (2.9)$$

where the effective Yukawa connecting the dark sector to the SM Higgs reads as $Y = \epsilon^n = \left(\frac{\langle\phi\rangle}{\Lambda}\right)^n$. We have already argued in introduction about our construction of dark matter sector. The idea of introducing vector-like fermions in the dark sector is also motivated by the fact that we expect a replication of the SM Yukawa type interaction to be present in the dark sector as well. Here the ϕ field plays the role of the messenger field similar to the one considered in [33]. See also [34–44] for some earlier efforts to relate A_4 flavor symmetry to DM. Note that the vev of the ϕ field is also instrumental in producing the term d to the neutrino mass matrix along with the vev of η . Since the d -term is responsible for generation of nonzero θ_{13} (will be discussed in the next section) a connection between non-zero $\sin \theta_{13}$ and DM interaction becomes correlated in our set-up.

A discussion about other possible terms allowed by the symmetries considered would be pertinent here. Terms like $\bar{\psi}\psi H^\dagger H/\Lambda$ and $\bar{\chi}^0\chi^0 H^\dagger H/\Lambda$ are actually allowed in the present set-up. However it turns out that their role is less significant compared to the other terms present. The reason is the following: firstly they could contribute to bare mass terms of ψ and χ^0 fields. However these contribution being proportional to v^2/Λ are insignificant as compared to M_ψ and M_χ . Similar conclusion holds for the Yukawa term as well. Secondly, they could take part in the DM annihilation. However as we will see, there also they do not have significant contribution because of the Λ suppression.

3 Phenomenology of the neutrino sector

Combining Eqs. (2.2) and (2.7), we get the light neutrino mass matrix as $m_\nu = (m_\nu)_0 + \delta m_\nu$. We have already seen that $(m_\nu)_0$ can be diagonalized by U_{TB} alone. Hence including δm_ν , rotation by U_{TB} results into the following structure of neutrino mass matrix:

$$m'_\nu = U_{TB}^T m_\nu U_{TB}, \quad (3.1)$$

$$= \begin{pmatrix} a - b - d/2 & 0 & \sqrt{3}d/2 \\ 0 & a + d & 0 \\ \sqrt{3}d/2 & 0 & -a - b + d/2 \end{pmatrix}. \quad (3.2)$$

So an additional rotation (by the U_1 matrix given below) is required to diagonalize m_ν ,

$$(U_{TB}U_1)^T m_\nu (U_{TB}U_1) = \text{diag}(m_1 e^{i\gamma_1}, m_2 e^{i\gamma_2}, m_3 e^{i\gamma_3}) \quad (3.3)$$

where

$$U_1 = \begin{pmatrix} \cos \theta_\nu & 0 & \sin \theta_\nu e^{-i\varphi} \\ 0 & 1 & 0 \\ -\sin \theta_\nu e^{i\varphi} & 0 & \cos \theta_\nu \end{pmatrix}. \quad (3.4)$$

Here $m_{i=1,2,3}$ are the real and positive eigenvalues and $\gamma_{i=1,2,3}$ are the phases associated to these mass eigenvalues. We can therefore extract the neutrino mixing matrix U_ν as,

$$U_\nu = U_{TB}U_1U_m = \begin{pmatrix} \sqrt{\frac{2}{3}}\cos\theta_\nu & \frac{1}{\sqrt{3}} & \sqrt{\frac{2}{3}}e^{-i\varphi}\sin\theta_\nu \\ -\frac{\cos\theta_\nu}{\sqrt{6}} + \frac{e^{i\varphi}\sin\theta_\nu}{\sqrt{2}} & \frac{1}{\sqrt{3}} & -\frac{\cos\theta_\nu}{\sqrt{2}} - \frac{e^{-i\varphi}\sin\theta_\nu}{\sqrt{6}} \\ -\frac{\cos\theta_\nu}{\sqrt{6}} - \frac{e^{i\varphi}\sin\theta_\nu}{\sqrt{2}} & \frac{1}{\sqrt{3}} & \frac{\cos\theta_\nu}{\sqrt{2}} - \frac{e^{-i\varphi}\sin\theta_\nu}{\sqrt{6}} \end{pmatrix} U_m, \quad (3.5)$$

where $U_m = \text{diag}(1, e^{i\alpha_{21}/2}, e^{i\alpha_{31}/2})$ is the Majorana phase matrix with $\alpha_{21} = (\gamma_1 - \gamma_2)$ and $\alpha_{31} = (\gamma_1 - \gamma_3)$, one common phase being irrelevant. The angle θ_ν and phase φ associated in U_1 can now be linked with the parameters: a, b, d involved in m_ν through Eq. (3.2).

Note that the parameters: a, b and d are all in general complex quantities. We define the phases associated with a, b, d as ϕ_a, ϕ_b and ϕ_d respectively. Also for simplifying the

analysis, we consider $|y_1| = |y_3| = y$ and $|y_2| = k$. With these, θ_ν and φ can be expressed in terms of the parameters involved in the effective light neutrino mass matrix m'_ν as:

$$\tan 2\theta_\nu = \frac{\sqrt{3}\epsilon \cos \phi_{db}}{(\epsilon \cos \phi_{db} - 2 \cos \phi_{ab}) \cos \varphi}, \quad (3.6)$$

$$\tan \varphi = \frac{y \sin(\phi_{db} - \phi_{ab})}{k \cos \phi_{db}}. \quad (3.7)$$

where $\phi_{ab} = \phi_a - \phi_b$ and $\phi_{db} = \phi_d - \phi_b$. Then comparing the standard U_{PMNS} parametrization and neutrino mixing matrix $U_\nu (= U_{TBM} U_1 U_m)$ we obtain

$$\sin \theta_{13} = \sqrt{\frac{2}{3}} |\sin \theta_\nu|, \quad \delta = \arg[(U_1)_{13}]. \quad (3.8)$$

From Eq. (3.6) and (3.7) it is clear that, $\sin \theta_\nu$ may take positive or negative value depending on the choices of ϵ and y/k . For $\sin \theta_\nu > 0$, we find $\delta = \varphi$ using $\delta = \arg[(U_1)_{13}]$. On the other hand for $\sin \theta_\nu < 0$; δ and φ are related by $\delta = \varphi \pm \pi$. Therefore in both these cases we obtain $\tan \varphi = \tan \delta$ and hence Eq. (3.7) leads to

$$\tan \delta = \frac{y \sin(\phi_{db} - \phi_{ab})}{k \cos \phi_{db}}. \quad (3.9)$$

The other two mixing angles follow the standard correlation with θ_{13} in A_4 models [24, 45].

Using Eq. (3.3), the complex light neutrino mass eigenvalues are evaluated as

$$m_{1,3}^c = \left[-b \pm \sqrt{a^2 - ad + d^2} \right], \quad (3.10)$$

$$m_2^c = (a + d). \quad (3.11)$$

Correspondingly the real and positive mass eigenvalues of light neutrinos are determined as

$$m_1 = \alpha \frac{y}{k} \left[\left(P - \frac{k}{y} \right)^2 + Q^2 \right]^{1/2}, \quad (3.12)$$

$$m_2 = \alpha \frac{y}{k} \left[1 + \epsilon^2 + 2\epsilon \cos(\phi_{ab} - \phi_{db}) \right]^{1/2}, \quad (3.13)$$

$$m_3 = \alpha \frac{y}{k} \left[\left(P + \frac{k}{y} \right)^2 + Q^2 \right]^{1/2}, \quad (3.14)$$

where

$$\alpha = \frac{k}{\Lambda} v^2 \epsilon, \quad P = \left[\frac{1}{2} (A + \sqrt{A^2 + B^2}) \right]^{1/2} \quad \text{and} \quad Q = \left[\frac{1}{2} (-A + \sqrt{A^2 + B^2}) \right]^{1/2}, \quad (3.15)$$

with

$$A = (\cos 2\phi_{ab} + \epsilon^2 \cos 2\phi_{db} - \epsilon \cos(\phi_{ab} + \phi_{db})), \quad (3.16)$$

$$B = (\sin 2\phi_{ab} + \epsilon^2 \sin 2\phi_{db} - \epsilon \sin(\phi_{ab} + \phi_{db})). \quad (3.17)$$

Also, phases (γ_i) associated with each mass eigenvalues can be expressed as

$$\gamma_1 = \phi_b + \tan^{-1} \left(\frac{Q}{P - \frac{k}{y}} \right), \quad (3.18)$$

$$\gamma_2 = \phi_b + \tan^{-1} \left(\frac{\sin \phi_{ab} + \epsilon \sin \phi_{db}}{\cos \phi_{ab} + \epsilon \cos \phi_{db}} \right), \quad (3.19)$$

$$\gamma_3 = \pi + \phi_b + \tan^{-1} \left(\frac{Q}{P + \frac{k}{y}} \right). \quad (3.20)$$

Using the above expressions of absolute neutrino masses, we define the ratio of solar to atmospheric mass-squared differences as r ,

$$r = \frac{\Delta m_{\odot}^2}{|\Delta m_{atm}^2|}, \quad (3.21)$$

with $\Delta m_{\odot}^2 \equiv \Delta m_{21}^2 = m_2^2 - m_1^2$ and $|\Delta m_{atm}^2| \equiv |\Delta m_{31}^2| = |m_3^2 - m_1^2|$. Then it turns out that both r and θ_{13} depends on $\epsilon, y/k$ and the relative phases: ϕ_{ab}, ϕ_{db} . The Dirac CP phase δ is also a function of these parameters only. As values of r and θ_{13} are precisely known from neutrino oscillation data, it would be interesting to constrain the parameter space of $\epsilon, y/k$ and the relative phases which can be useful in predicting δ . However analysis with all these four parameters is difficult to perform. So, below we categorize few cases depending on some specific choices of relative phases. In doing the analysis, following [14], the best fit values of $\Delta m_{\odot}^2 = 7.6 \times 10^{-5} \text{ eV}^2$ and $|\Delta m_{atm}^2| = 2.48 \times 10^{-3} \text{ eV}^2$ are used for our analysis. r and $\sin \theta_{13}$ are taken as 0.03 and 0.1530 (best fit value [14]) respectively.

3.1 Case A : $\phi_{ab} = \phi_{db} = 0$

Here we make the simplest choice for the phases, $\phi_{ab} = \phi_{db} = 0$. Then the Eq. (3.6) becomes function of ϵ alone [28] as:

$$\tan 2\theta_{\nu} = \frac{\sqrt{3}\epsilon}{\epsilon - 2}. \quad (3.22)$$

Hence $\sin \theta_{13}$ depends only on ϵ where following Eq. (3.9), the Dirac CP phase is zero or π . The ϵ dependence of $\sin \theta_{13}$ is represented in Fig. 1. The horizontal patch in Fig. 1 denotes the allowed 3σ range of $\sin \theta_{13}$ ($\equiv 0.1330$ - 0.1715) [14] which is in turn restrict the range of ϵ parameter (between 0.328 and 0.4125) denoted by the vertical patch in the same figure. Note that the interaction strength of DM with the SM particles depends on $\epsilon^n \equiv Y$. Therefore we find that the size of $\sin \theta_{13}$ is intimately related with the Higgs portal coupling of DM. This is the most significant observation of this paper. With the above mentioned range of ϵ , obtained from Fig. 1, the two other mixing angles θ_{12} and θ_{23} are found to be within the 3σ range.

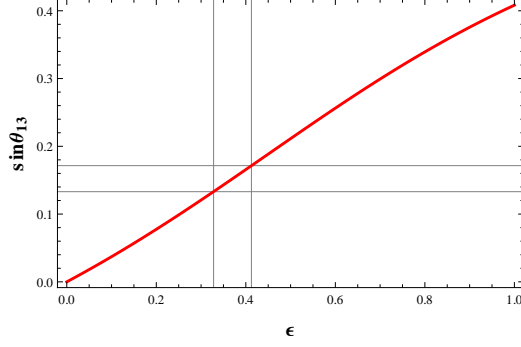


Figure 1. Plot of $\sin \theta_{13}$ against ϵ . 3σ range [14] of $\sin \theta_{13}$ (indicated by the horizontal lines) fixes ϵ in the range: 0.328-0.4125 (indicated by vertical lines).

Expressions for the real and positive mass eigenvalues are obtained from Eq. (3.12-3.14) and can be written as

$$m_1 = \alpha \frac{y}{k} \left| \sqrt{1 - \epsilon + \epsilon^2} - k/y \right|, \quad (3.23)$$

$$m_2 = \alpha \frac{y}{k} [1 + \epsilon], \quad (3.24)$$

$$m_3 = \alpha \frac{y}{k} \left[\sqrt{1 - \epsilon + \epsilon^2} + k/y \right]. \quad (3.25)$$

With the above mass eigenvalues, one can write the ratio of solar to atmospheric mass-squared differences as defined in Eq. (3.21) as:

$$r = \frac{3\epsilon \frac{y}{k} - \frac{k}{y} + 2\sqrt{1 - \epsilon + \epsilon^2}}{4\sqrt{1 - \epsilon + \epsilon^2}}. \quad (3.26)$$

From Fig. 1, we have fixed ϵ range corresponding to 3σ range of $\sin \theta_{13}$. Now, to satisfy $r = 0.03$ [14], we vary the ratio of the coupling constants, y/k , against ϵ using Eq. (3.21) and (3.23-3.25). The result is presented in Fig. 2. The vertical patch there represents

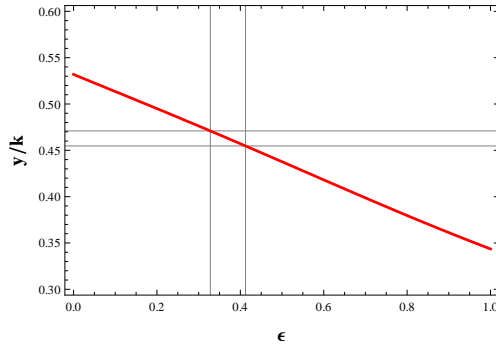


Figure 2. Contour plot of $r = 0.03$ in $y/k - \epsilon$ plane. The vertical lines represent the allowed range for ϵ (0.328-0.4125) corresponding to 3σ range of $\sin \theta_{13}$ which restricts the ratio y/k between 0.471 to 0.455 indicated by horizontal lines.

allowed region for ϵ fixed from Fig. 1 which determines the range of y/k to be within 0.471-0.455. After obtaining ϵ and the ratio y/k , we can now find the factor k/Λ (within α) in order to satisfy the solar mass-squared difference $\Delta m_{\odot}^2 = m_2^2 - m_1^2 = 7.6 \times 10^{-5} \text{ eV}^2$ [14]. Using Eq. (3.23) and (3.24) we find this factor to be

$$\frac{k}{\Lambda} = \frac{1}{v^2 \epsilon \frac{y}{k}} \sqrt{\frac{\Delta m_{\odot}^2}{\left[3\epsilon - \left(\frac{k}{y}\right)^2 + 2\frac{k}{y} \sqrt{1 + \epsilon^2 - \epsilon} \right]}}. \quad (3.27)$$

Considering the 3σ variation of $\sin \theta_{13}$, it falls within $1.97 \times 10^{-15} \text{ GeV}^{-1}$ to $1.60 \times 10^{-15} \text{ GeV}^{-1}$ with $v = 246 \text{ GeV}$. Once we know about all parameters involved like $\epsilon, y/k, k/\Lambda$

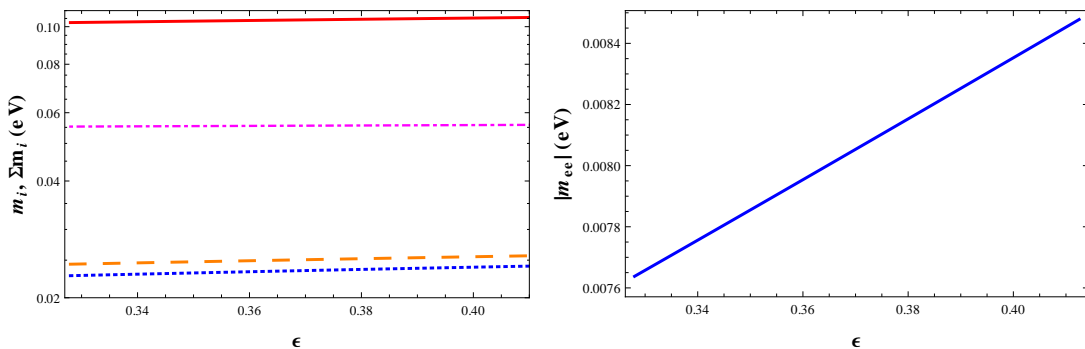


Figure 3. Left: Individual absolute neutrino masses (m_1 - blue dotted line, m_2 - orange dashed line, m_3 - magenta dot-dashed line) and their sum (continuous red line) against ϵ (0.328-0.4125) corresponding to 3σ range of $\sin \theta_{13}$. Right: Effective neutrino mass parameter (continuous blue line) against ϵ (0.328-0.4125) corresponding to 3σ range of $\sin \theta_{13}$.

Parameters/Observable	Allowed Range
ϵ	0.328-0.4125
k/Λ (GeV^{-1})	$1.97 \times 10^{-15} - 1.60 \times 10^{-15}$
Σm_i (eV)	0.102 - 0.106
$ m_{ee} $ (eV)	0.00764-0.00848

Table 2. Range of $\epsilon, k/\Lambda, \Sigma m_i, |m_{ee}|$ for 3σ range of $\sin \theta_{13}$ with $\phi_{ab} = \phi_{db} = 0$.

with the specific choice of the phases (in this case $\phi_{ab} = \phi_{db} = 0$), it is straightforward to determine absolute neutrino masses and effective neutrino mass parameter involved in neutrinoless double beta decay using

$$|m_{ee}| = \left| m_1^2 c_{12}^2 c_{13}^2 + m_2^2 s_{12}^2 c_{13}^2 e^{i\alpha_{21}} + m_3^2 s_{13}^2 e^{i(\alpha_{31} - 2\delta)} \right| \quad (3.28)$$

as shown in Fig. 3. We also have listed the summary of the predictions of these quantities in Table 2.

3.2 Case B : $\phi_{db} = 0$

Now we consider the case: $\phi_{db} = 0$. Then the relations for θ_ν and δ take the form

$$\tan 2\theta_\nu = \frac{\sqrt{3}\epsilon}{(\epsilon - 2 \cos \phi_{ab}) \cos \varphi}, \quad (3.29)$$

$$\tan \delta = -\frac{y}{k} \sin \phi_{ab}. \quad (3.30)$$

So from Eqs. (3.8, 3.29-3.30) and since $\tan \delta = \tan \varphi$, it is clear that unlike the Case A, here $\sin \theta_{13}$ depends not only on ϵ and y/k but also on the phase present in the theory, *i.e.* ϕ_{ab} . Therefore there would exist a one to one correspondence between ϵ and y/k in order to produce a specific value of $\sin \theta_{13}$ once a particular choice of δ has been made.

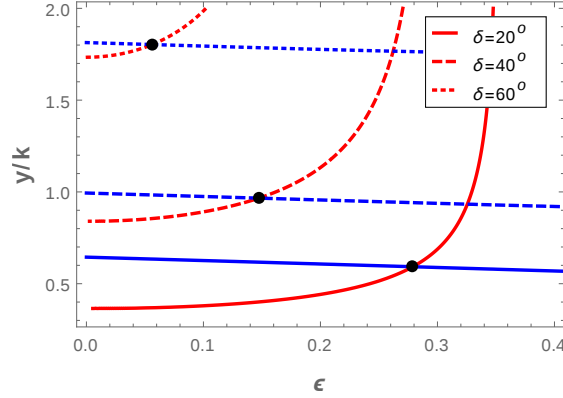


Figure 4. Contour plots for both $\sin \theta_{13} = 0.1530$ (shown in red continuous, dashed and dotted lines) and $r = 0.03$ (shown in blue continuous, dashed and dotted lines) for $\delta = 20^\circ, \delta = 40^\circ$ and $\delta = 60^\circ$ respectively in ϵ - y/k plane. Black dots on each intersection represents solution for ϵ and y/k corresponding to each δ for $\phi_{db} = 0$.

Now, with $\phi_{db} = 0$, absolute neutrino masses given in Eq. (3.12-3.14) are reduced to

$$m_1 = \alpha \frac{y}{k} \left[\left(P_1 - \frac{k}{y} \right)^2 + Q_1^2 \right]^{1/2}, \quad (3.31)$$

$$m_2 = \alpha \frac{y}{k} \left[1 + \epsilon^2 + 2\epsilon \cos \phi_{ab} \right]^{1/2}, \quad (3.32)$$

$$m_3 = \alpha \frac{y}{k} \left[\left(P_1 + \frac{k}{y} \right)^2 + Q_1^2 \right]^{1/2}, \quad (3.33)$$

with

$$P_1 = \left[\frac{1}{2} (A_1 + \sqrt{A_1^2 + B_1^2}) \right]^{1/2}, \quad Q_1 = \left[\frac{1}{2} (-A_1 + \sqrt{A_1^2 + B_1^2}) \right]^{1/2}, \quad (3.34)$$

$$A_1 = (\epsilon^2 + \cos 2\phi_{ab} - \epsilon \cos \phi_{ab}) \text{ and } B_1 = (\sin 2\phi_{ab} - \epsilon \sin \phi_{ab}). \quad (3.35)$$

The ratio of solar to atmospheric neutrino mass-squared differences takes the form

$$r = \frac{1}{4P_1 \frac{k}{y}} \left[(1 + \epsilon^2 + 2\epsilon \cos \phi_{ab}) - \left(P_1 - \frac{k}{y} \right)^2 - Q_1^2 \right]. \quad (3.36)$$

Clearly, one finds that ϵ and y/k are the only parameters involved in both $\sin\theta_{13}$ and r once δ values are taken as input. Therefore, those values of ϵ and y/k are allowed which simultaneously satisfy data obtained for $\sin\theta_{13}$ and r from neutrino oscillation experiments. Here we have considered the best fit values from [14] and drawn contour plots for $\sin\theta_{13} = 0.1530$ and $r = 0.03$. Intersection of these contours then represents solutions for ϵ and y/k . Note that $\delta = 0$ case corresponds to the results obtained in Case A.

In Fig. 4, we have plotted typical contours obtained for $\sin\theta_{13} = 0.1530$ (red lines) and $r = 0.03$ (blue lines) for $\delta = 20^\circ, \delta = 40^\circ$ and $\delta = 60^\circ$ respectively in ϵ - y/k plane. The intersecting points are denoted by black dots and represent the solution points for ϵ and y/k . In Table 3 we have listed estimations for ϵ and y/k for different δ values. Just

δ	ϵ	y/k	k/Λ (10^{-15} GeV $^{-1}$)	Σm_i (eV)	$ m_{ee} $ (eV)
0°	0.372	0.463	1.756	0.1042	0.0222
10°	0.343	0.496	1.910	0.1068	0.0236
20°	0.279	0.592	2.361	0.1143	0.0274
30°	0.209	0.745	3.140	0.1267	0.0331
40°	0.147	0.966	4.405	0.1454	0.0409
50°	0.096	1.288	6.610	0.1743	0.0516
60°	0.056	1.803	11.10	0.2230	0.0682
61°	0.053	1.873	11.80	0.2298	0.0704
70°	0.026	2.798	23.22	0.3210	0.1002
80°	0.007	5.743	85.42	0.6173	0.1952

Table 3. Estimated values of various parameters and observables satisfying neutrino oscillation data for different values of δ with $\phi_{db} = 0$.

like the previous case, after obtaining ϵ and y/k , we can find the factor k/Λ using the fact that it has to produce correct solar mass-squared difference $\Delta m_\odot^2 = m_2^2 - m_1^2 = 7.6 \times 10^{-5}$ eV 2 [14]. For this, we employ Eq. (3.31) and (3.32). All these findings are mentioned in Table 3 including sum of the absolute masses (Σm_i) of all three light neutrinos and effective neutrino mass parameter involved in neutrinoless double beta decay ($|m_{ee}|$) for different considerations of leptonic CP phase δ . In this analysis we observe that, for various values of δ between 0° to 360° there are certain points where same set of solutions for ϵ and y/k are repeated (*e.g.* solutions with δ is repeated for $|\pi - \delta|$). We should also employ the upper bound of sum of all three light neutrino masses ($\Sigma m_i < 0.23$ eV) coming from cosmological observation by Planck [6]. Once this is included, we note that some of the δ values need to be discarded as the corresponding sum of the masses exceeds 0.23 eV as seen from Table 3. We therefore conclude that the allowed values for δ are: between $0^\circ - 61^\circ$ (and also $119^\circ - 180^\circ, 180^\circ - 241^\circ$ and $299^\circ - 360^\circ$).

3.3 Case C : $\phi_{ab} = 0$

When $\phi_{ab} = 0$, relations for θ_ν and δ take the form

$$\tan 2\theta_\nu = \frac{\sqrt{3}\epsilon \cos \phi_{db}}{(\epsilon \cos \phi_{db} - 2) \cos \varphi}, \quad (3.37)$$

$$\tan \delta = \frac{y}{k} \tan \phi_{ab}. \quad (3.38)$$

Here also $\sin \theta_{13}$ depends on $\epsilon, y/k$ and the phase involved ϕ_{db} . The real and positive mass eigenvalues can be written as

$$m_1 = \alpha \frac{y}{k} \left[\left(P_2 - \frac{k}{y} \right)^2 + Q_2^2 \right]^{1/2}, \quad (3.39)$$

$$m_2 = \alpha \frac{y}{k} \left[1 + \epsilon^2 + 2\epsilon \cos \phi_{db} \right]^{1/2}, \quad (3.40)$$

$$m_3 = \alpha \frac{y}{k} \left[\left(P_2 + \frac{k}{y} \right)^2 + Q_2^2 \right]^{1/2}, \quad (3.41)$$

with

$$P_2 = \left[\frac{1}{2} (A_2 + \sqrt{A_2^2 + B_2^2}) \right]^{1/2}, \quad Q_2 = \left[\frac{1}{2} (-A_2 + \sqrt{A_2^2 + B_2^2}) \right]^{1/2}, \quad (3.42)$$

where

$$A_2 = (1 + \epsilon^2 \cos 2\phi_{db} - \epsilon \cos \phi_{db}) \text{ and } B_2 = (\epsilon^2 \sin 2\phi_{db} - \epsilon \sin \phi_{db}). \quad (3.43)$$

The ratio of solar to atmospheric neutrino mass-squared differences takes the form

$$r = \frac{y/k}{4P_2} \left[(1 + \epsilon^2 + 2\epsilon \cos \phi_{db}) - (P_2 - k/y)^2 - Q_2^2 \right]. \quad (3.44)$$

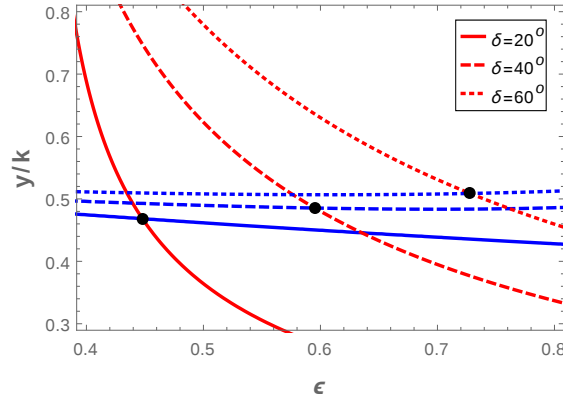


Figure 5. Contour plots for both $\sin \theta_{13} = 0.1530$ (shown in red continuous, dashed and dotted lines) and $r = 0.03$ (shown in blue continuous, dashed and dotted lines) for $\delta = 20^\circ, \delta = 40^\circ$ and $\delta = 60^\circ$ respectively in ϵ - y/k plane. Black dots on each intersection represents solution for ϵ and y/k corresponding to each δ for $\phi_{ab} = 0$.

We then scan the parameter space for ϵ and y/k for various choices of δ so as to have $r = 0.03$ and $\sin \theta_{13} = 0.153$. In Fig. 5, we provide contour plots for $\sin \theta_{13} = 0.1530$ (red lines) and $r = 0.03$ (blue lines) for $\delta = 20^\circ, \delta = 40^\circ$ and $\delta = 60^\circ$. The intersection between $\sin \theta_{13}$ and r contours indicate the simultaneous satisfaction of them. Hence the intersections are indicated by black dots with which a pair of $\epsilon, y/k$ are attached. Similar to the previous two cases, here we estimate the k/Λ for each such pair of $\epsilon, y/k$ with a specific δ . This in turn provide an estimate of Σm_i and effective mass parameter $|m_{ee}|$ depending on the choice of δ . We provide these outcomes in Table 4.

δ	ϵ	y/k	k/Λ ($10^{-15} \text{ GeV}^{-1}$)	Σm_i (eV)	$ m_{ee} $ (eV)
0°	0.372	0.463	1.756	0.1042	0.0222
10°	0.393	0.464	1.670	0.1048	0.0225
20°	0.448	0.468	1.480	0.1065	0.0233
30°	0.520	0.475	1.300	0.1093	0.0245
40°	0.595	0.485	1.167	0.1128	0.0260
50°	0.666	0.497	1.065	0.1162	0.0273
60°	0.728	0.509	0.981	0.1182	0.0280
70°	0.782	0.519	0.901	0.1179	0.0275
80°	0.827	0.526	0.826	0.1152	0.0259

Table 4. Estimated values of various parameters and observables satisfying neutrino oscillation data for different values of δ with $\phi_{ab} = 0$.

3.4 Case D : $\phi_{ab} = \phi_{db} = \beta$

With $\phi_{ab} = \phi_{db} = \beta$, the mixing angle θ_ν turns out to be function of ϵ only and is given by

$$\tan 2\theta_\nu = \frac{\sqrt{3}\epsilon}{\epsilon - 2}, \quad (3.45)$$

while $\tan \delta$ becomes zero. Note that the expressions for the mixing angle θ_ν and δ are identical to the ones obtained in Case A. Therefore we use the constraint on ϵ obtained from Fig. 1 in order to satisfy 3σ allowed range of $\sin \theta_{13}$. However the expressions for real and positive mass eigenvalues involve the common phase β and can be written as (following Eqs. (3.12-3.14))

$$m_1 = \alpha \frac{y}{k} \left[\left(\sqrt{1 - \epsilon + \epsilon^2} \cos \beta - \frac{k}{y} \right)^2 + \left(\sqrt{1 - \epsilon + \epsilon^2} \sin \beta \right)^2 \right]^{1/2}, \quad (3.46)$$

$$m_2 = \alpha \frac{y}{k} [1 + \epsilon], \quad (3.47)$$

$$m_3 = \alpha \frac{y}{k} \left[\left(\sqrt{1 - \epsilon + \epsilon^2} \cos \beta + \frac{k}{y} \right)^2 + \left(\sqrt{1 - \epsilon + \epsilon^2} \sin \beta \right)^2 \right]^{1/2}. \quad (3.48)$$

Then following our approach for finding the range of parameters which would satisfy the

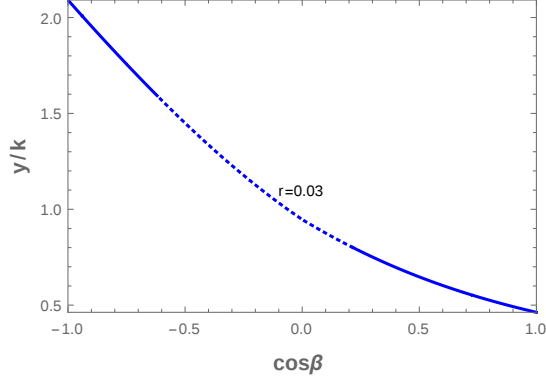


Figure 6. Contour plot for $r = 0.03$ in the $y/k - \cos \beta$ plane for $\phi_{db} = \phi_{ab} = \beta$. The disallowed range of $y/k, \cos \beta$ is indicated by the dotted portion.

oscillation parameters obtained from experimental data, we define the ratio of solar to atmospheric mass-squared differences as defined in Eq. (3.21) as

$$r = \frac{3\epsilon \frac{y}{k} - \frac{k}{y} + 2 \cos \beta \sqrt{1 - \epsilon + \epsilon^2}}{4 |\cos \beta| \sqrt{1 - \epsilon + \epsilon^2}}. \quad (3.49)$$

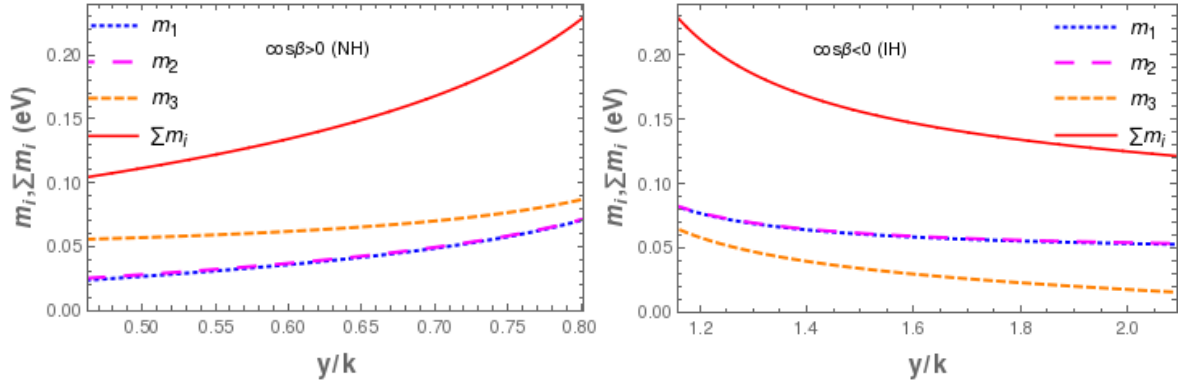


Figure 7. Absolute neutrino masses vs y/k (blue dotted, magenta large-dashed, orange dashed and red continuous lines represent m_1, m_2, m_3 and $\sum m_i$ respectively). The left panel is for $\cos \beta > 0$ and right panel is for $\cos \beta < 0$.

From Fig. 1 we fix $\epsilon = 0.372$ which would produce the best fit value of $\sin \theta_{13}$. Then, using the ratio of solar to atmospheric mass squared difference as given in Eq. (3.49), we can constrain y/k and $\cos \beta$. Here we plot $r = 0.03$ contour in the $y/k - \cos \beta$ plane as shown in Fig. 6. For $-1 \leq \cos \beta \leq 1$. We observe that y/k falls within the range: $0.463 \leq y/k \leq 2.091$. Thus Fig. 6 establishes a correlation between y/k and $\cos \beta$. Now to find absolute neutrino masses we need to obtain k/Λ first. We can find k/Λ from the

best fit value for solar mass squared difference, $m_2^2 - m_1^2 = 7.6 \times 10^{-5} \text{ eV}^2$, and is given by

$$\left(\frac{k}{\Lambda}\right)^2 = \frac{\Delta m_{\odot}^2}{4r(v^2\epsilon)^2 y/k |\cos\beta| \sqrt{1 + \epsilon^2 - \epsilon}}. \quad (3.50)$$

We have used Eq. (3.46-3.48) to obtain the above equation. Once ϵ is fixed at 0.372 and following Fig. 6 we know y/k and corresponding $\cos\beta$ (to have $r = 0.03$), we can use Eq. (3.50) to have an estimate for k/Λ . Now by knowing k/Λ , we have plotted absolute masses for light neutrinos in Fig. 7 by using Eq. (3.46-3.48). Here the left (right) panel is for $\cos\beta > 0 (< 0)$ and indicates normal (inverted) hierarchy for light neutrino masses. In Fig. 7, absolute neutrino masses m_1, m_2, m_3 and $\sum m_i$ are denoted by blue dotted, magenta large-dashed, orange dashed and red continuous lines respectively. Note that here we have plotted sum of the three absolute light neutrino masses consistent with the recent observation made by PLANCK, *i.e.* $\sum m_i \leq 0.23 \text{ eV}$ [6]. If we impose this constraint on the sum of absolute masses of the three light neutrinos, then the allowed region for y/k gets further constrained. The dotted portion in Fig. 6 represents this excluded part. Therefore the allowed region for y/k then turns out to be $0.463 \leq y/k \leq 0.802$ for $\cos\beta > 0$ (normal hierarchy) and $1.159 \leq y/k \leq 2.091$ for $\cos\beta < 0$ (inverted hierarchy). Finally in this case, the prediction for $|m_{ee}|$ found to be within $0.022 \text{ eV} < |m_{ee}| < 0.039 \text{ eV}$ for normal hierarchy and $0.016 \text{ eV} < |m_{ee}| < 0.035 \text{ eV}$ for inverted hierarchy.

4 Phenomenology of DM Sector

The dark sector consists of two vector-like fermions: a fermion doublet ψ and a singlet χ . The corresponding Lagrangian respecting the $U(1)$ and other discrete symmetries is provided in Eq. (2.9). At this stage we can remind ourselves about the minimality of the construction in terms of choice of constituents of the dark sector. Note that a vector-like singlet fermion alone can not have a coupling with the SM sector at the renormalizable level and thereby its relic density is expected to be over abundant (originated from interaction suppressed by the new physics scale Λ). On the contrary, a vector-like fermion doublet alone can have significant annihilation cross section from its gauge interaction with the SM sector and thereby we would expect the corresponding dark matter relic density to be under-abundant unless the DM mass is exorbitantly high. Hence we can naturally ask the question whether involvement of a singlet and a doublet vector-like fermions can lead to the dark matter relic density at an acceptable level. It then crucially depends on the mixing term between the singlet and the doublet fermions, *i.e.* on $m_D = Yv$. We expect a rich phenomenology out of it particularly because the coupling Y depends on the parameter ϵ through $Y = \epsilon^n$ where ϵ plays an important role in the neutrino physics as evident from our discussion in the previous section. We aim to restrict n phenomenologically.

The electroweak phase transition along with the $U(1)$ breaking give rise to the following mass matrix in the basis (χ^0, ψ^0)

$$\mathcal{M} = \begin{pmatrix} M_\chi & m_D \\ m_D & M_\psi \end{pmatrix}. \quad (4.1)$$

We obtain mass eigenstates ψ_1 and ψ_2 with masses M_1 and M_2 respectively after diagonalization of the above matrix as

$$\begin{aligned}\psi_1 &= \cos \theta_d \chi^0 + \sin \theta_d \psi^0, \\ \psi_2 &= \cos \theta_d \psi^0 - \sin \theta_d \chi^0,\end{aligned}\tag{4.2}$$

where $\tan 2\theta_d = 2m_D/(M_\psi - M_\chi)$. We will work in the regime where $m_D \ll M_\psi, M_\chi$. This choice would be argued soon. However this is not unnatural as the dark matter is expected to interact weakly. In this limit, the mass eigenvalues are found to be

$$\begin{aligned}M_1 &\approx M_\chi - \frac{m_D^2}{M_\psi - M_\chi}, \\ M_2 &\approx M_\psi + \frac{m_D^2}{M_\psi - M_\chi}.\end{aligned}\tag{4.3}$$

In this small mixing limit, we can write $M_\psi - M_\chi \simeq M_2 - M_1 = \Delta M$. Therefore the mixing angle θ_d can be approximately represented by

$$\sin 2\theta_d \simeq \frac{2Yv}{\Delta M}.\tag{4.4}$$

Then as evident from Eqs. (4.2), ψ_1 is dominantly the singlet having a small admixture with the doublet. We assume it to be the lightest between the two (*i.e.* $M_1 < M_2$) and forms the DM component of the universe. In the physical spectrum, we also have a charged fermion $\psi^+(\psi^-)$ with mass $M^+(M^-) = M_1 \sin^2 \theta_d + M_2 \cos^2 \theta_d$. In the limit $\theta_d \rightarrow 0$, $M^\pm = M_2 = M_\psi$. In this section, we will discuss the relic density of dark matter as a function of Y . Although Y represents Yukawa coupling of the DM with SM Higgs, in presence of a singlet and doublet fermions, Y is also a function of the mixing angle $\sin \theta_d$ as well as the mass splitting (ΔM as in Eq. (4.4)) which crucially controls DM phenomenology as we demonstrate in the following discussion.

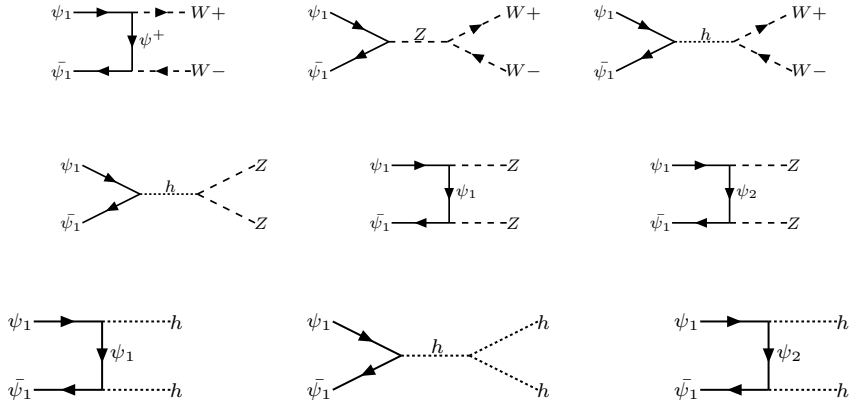


Figure 8. Dominant Annihilation processes to Higgs and Gauge boson final states.

Note that ψ_0 being the gauge doublet, it carries the gauge interactions and hence, the physical mass eigenstates including the DM have the following interaction with Z, W bosons as :

$$\frac{g}{\sqrt{2}}\bar{\psi}_0\gamma^\mu W_\mu^+\psi^- + \text{h.c.} \rightarrow \frac{g \sin \theta_d}{\sqrt{2}}\bar{\psi}_1\gamma^\mu W_\mu^+\psi^- + \frac{g \cos \theta_d}{\sqrt{2}}\bar{\psi}_2\gamma^\mu W_\mu^+\psi^- + \text{h.c.}, \quad (4.5)$$

$$\frac{g}{2 \cos \theta_w}\bar{\psi}_0\gamma^\mu Z_\mu\psi_0 \rightarrow \frac{g}{2 \cos \theta_w} (\sin^2 \theta_d \bar{\psi}_1\gamma^\mu Z_\mu\psi_1 + \sin \theta_d \cos \theta_d (\bar{\psi}_1\gamma^\mu Z_\mu\psi_2 + \bar{\psi}_2\gamma^\mu Z_\mu\psi_1) + \cos^2 \theta_d \bar{\psi}_2\gamma^\mu Z_\mu\psi_2). \quad (4.6)$$

The relic density of the dark matter (ψ_1) is mainly dictated by annihilations through (i) $\bar{\psi}_1\psi_1 \rightarrow W^+W^-, ZZ$ through $SU(2)_L$ gauge coupling and (ii) $\bar{\psi}_1\psi_1 \rightarrow hh$ through Yukawa coupling introduced in Eq. (2.8). The relevant processes are indicated in Fig. 8. The other

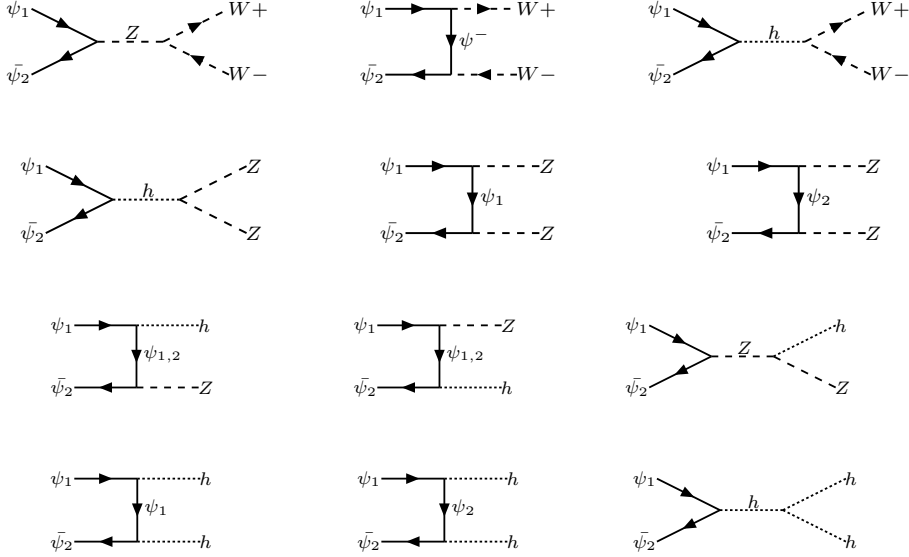


Figure 9. Dominant Co-Annihilations $\psi_1\bar{\psi}_2$ to Higgs and Gauge boson final states.

possible channels are mainly co-annihilation of ψ_1 with ψ_2 (see Fig. 9), ψ_1 with ψ^\pm (see Fig. 10) and annihilations of ψ^\pm (see Fig. 11) which would dominantly contribute to relic density in a large region of parameter space [19, 46–49] as can be seen once we proceed further. At this stage we can argue on our choice of making θ_d small, or in other words why the mixing with doublet is necessary to be small for the model to provide a DM with viable relic density. This is because the larger is the doublet content in DM ψ_1 , the annihilation goes up significantly in particular through $\psi_1\bar{\psi}_1 \rightarrow W^+W^-$ through Z and hence yielding a very small relic density. So in the small mixing limit, ψ_2 is dominantly a doublet having a mixture of minor singlet component. This implies that ψ_2 mass is required to be larger than 45 GeV in order not to be in conflict with the invisible Z -boson decay width.

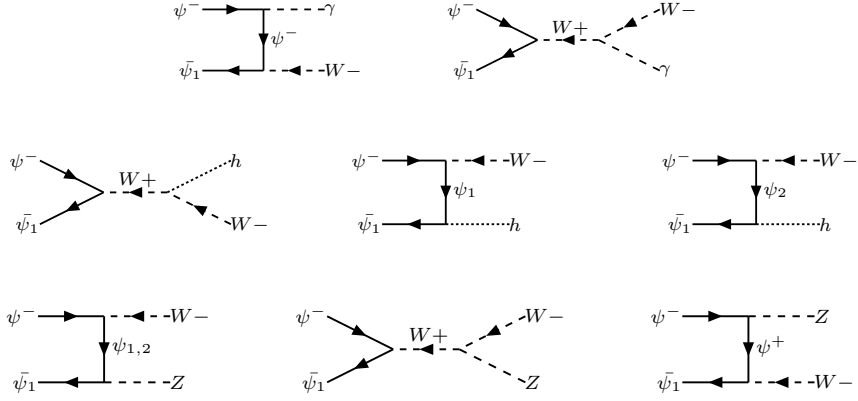


Figure 10. Dominant Co-Annihilation $\bar{\psi}_1\psi^-$ to Higgs and gauge boson final states.

The relic density of the ψ_1 DM with mass M_1 can be given by [46]

$$\Omega_{\psi_1} h^2 = \frac{1.09 \times 10^9 \text{ GeV}^{-1}}{g_\star^{1/2} M_{PL}} \frac{1}{J(x_f)}, \quad (4.7)$$

where $J(x_f)$ is given by

$$J(x_f) = \int_{x_f}^{\infty} \frac{\langle \sigma |v| \rangle_{eff}}{x^2} dx. \quad (4.8)$$

Here $\langle \sigma |v| \rangle_{eff}$ is the thermal average of dark matter annihilation cross sections including

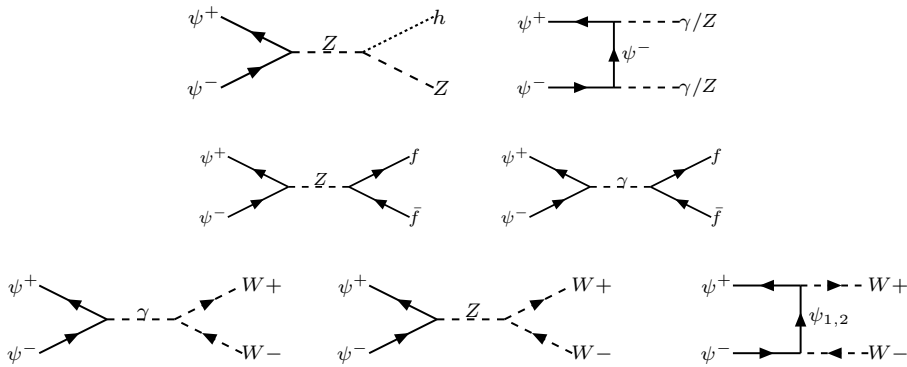


Figure 11. Dominant Co-Annihilation processes of $\psi^+\psi^- \rightarrow$ SM particles where f represents SM fermions.

contributions from co-annihilations as follows²:

$$\begin{aligned}
\langle\sigma|v|\rangle_{eff} &= \frac{g_1^2}{g_{eff}^2}\sigma(\bar{\psi}_1\psi_1) + 2\frac{g_1g_2}{g_{eff}^2}\sigma(\bar{\psi}_1\psi_2)(1+\Delta)^{3/2}\exp(-x\Delta) \\
&+ 2\frac{g_1g_3}{g_{eff}^2}\sigma(\bar{\psi}_1\psi^-)(1+\Delta)^{3/2}\exp(-x\Delta) \\
&+ 2\frac{g_2g_3}{g_{eff}^2}\sigma(\bar{\psi}_2\psi^-)(1+\Delta)^3\exp(-2x\Delta) + \frac{g_2g_2}{g_{eff}^2}\sigma(\bar{\psi}_2\psi_2)(1+\Delta)^3\exp(-2x\Delta) \\
&+ \frac{g_3g_3}{g_{eff}^2}\sigma(\psi^+\psi^-)(1+\Delta)^3\exp(-2x\Delta).
\end{aligned} \tag{4.9}$$

In the above equation g_1, g_2 and g_3 are the spin degrees of freedom for ψ_1 , ψ_2 and ψ^- respectively. Since these are spin half particles, all g 's are 2. The freeze-out of ψ_1 is parameterised by $x_f = \frac{M_1}{T_f}$, where T_f is the freeze out temperature. Δ depicts the mass splitting ratio as $\Delta = \frac{M_2 - M_1}{M_1} = \frac{\Delta M}{M_1}$, where M_2 stands for the mass of both ψ_2 and ψ^\pm . The effective degrees of freedom g_{eff} in Eq. (4.9) is given by

$$g_{eff} = g_1 + g_2(1 + \Delta)^{3/2}\exp(-x\Delta) + g_3(1 + \Delta)^{3/2}\exp(-x\Delta). \tag{4.10}$$

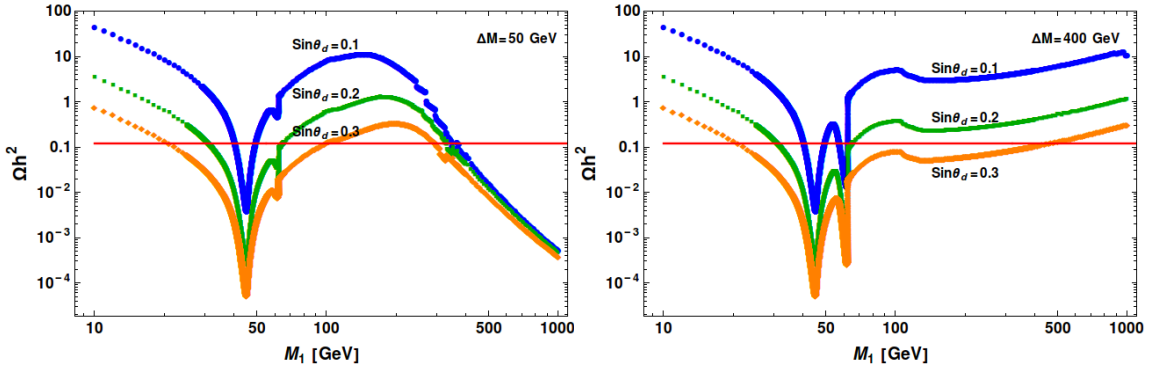


Figure 12. Relic density vs DM mass M_1 (in GeV) for different choices of $\sin\theta_d = \{0.1, 0.2, 0.3\}$ with $\Delta M = 50$ GeV [left] (corresponding to $Y = \{0.02, 0.04, 0.058\}$ with blue, green, orange respectively) and $\Delta M = 400$ GeV [right] (corresponding to $Y = \{0.16, 0.32, 0.46\}$ with Blue, Green, Orange respectively). Horizontal lines define the correct relic density.

As it turns out from the above discussion, the dark-sector phenomenology in our set-up is mainly dictated by three parameters $\sin\theta_d, M_1$ and ΔM . However we will keep on changing $\sin\theta_d$ and/or ΔM dependence with Y wherever required using Eq.(4.4). In the following we use the code `MicrOmegas` [50] to find the allowed region of correct relic abundance for our DM candidate ψ_1 satisfying PLANCK constraints [6, 7],

$$0.1175 \leq \Omega_{\text{DM}}h^2 \leq 0.1219. \tag{4.11}$$

²If M_2 is very close to M_1 then ψ_2 decay to ψ_1 should contribute to relic density. However the parameter space scan that we have performed with $\Delta M \gtrsim$ GeV, excludes such possibility.

In Fig. 12 we plot relic density versus DM mass M_1 for different choices of $\sin \theta_d = 0.1, 0.2$ and 0.3 (represented by blue, green and orange dotted lines respectively) while keeping the mass difference ΔM fixed at 50 GeV in the left panel and at $\Delta M = 400$ GeV in the right panel. The choice of various $\sin \theta_d$ can be translated into different values of Y as well, through Eq. (4.4) since ΔM is kept fixed. Then it is equivalent to say that the blue, green and orange dotted lines in the left panel ($\Delta M = 50$ GeV) represent $Y = 0.02, 0.04, 0.058$ respectively. In a similar way, the blue, green and orange dotted lines in the right panel ($\Delta M = 400$ GeV) represent $Y = 0.16, 0.32, 0.46$ respectively. We infer that as the mixing increases or in other words Y increases (ΔM is fixed), the doublet component starts to dominate (see Eq. (4.4)) and hence give larger cross-section which leads to a smaller DM abundance for a particular M_1 . The second important point to note is the presence of Z resonance at $M_1 = M_Z/2 \sim 45$ GeV and a Higgs resonance at $M_1 = M_H/2 \sim 63$ GeV where relic density drops sharply due to increase in annihilation cross-section. We can also see that with larger ΔM , *i.e.* with larger Y (as $\sin \theta_d$ is fixed) in the right hand side, the Higgs resonance is more prominent for obvious reasons. Relic density for these chosen parameters are satisfied across the Z resonance window and H resonance window (more prominent for larger ΔM on the right panel). For small $\Delta M = 50$ GeV (left panel of Fig. 12), relic density drops beyond DM mass of 300 GeV. This is due to co-annihilation channels start contributing $\bar{\psi}_2\psi_1 \rightarrow SM$ or $\bar{\psi}^+\psi_1 \rightarrow SM$ and we find that the relic density is satisfied for DM mass ~ 400 GeV. This is however not seen in the right panel where we have larger ΔM . This is because with the large mass gap, co-annihilation doesn't contribute significantly due to Boltzmann suppression for DM masses upto TeV. That is why with larger ΔM (right panel of Fig. 12), there is no point for DM mass beyond 100 GeV associated with smaller $\sin \theta_d$ values like 0.1, 0.2, where relic density constraint is satisfied. With larger $\sin \theta_d = 0.3$ one can satisfy relic density without the aid of co-annihilation for $M_1 \sim 500$ GeV. We also note a small drop in relic density on the right panel in particular, when WW and ZZ channels open up for annihilation.

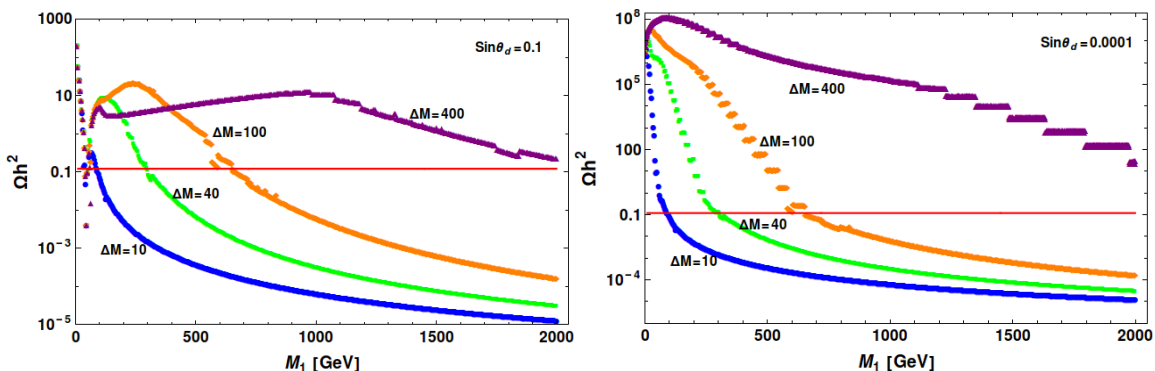


Figure 13. Left: Ωh^2 versus Dark matter mass M_1 (in GeV) for $\sin \theta_d = 0.1$ with different choices of $\Delta M = \{10, 40, 100, 400\}$ GeV described by $\{ \text{blue, green, orange, purple} \}$ respectively. Right: Same as left panel but with different $\sin \theta_d = 0.0001$. Horizontal lines indicate correct relic density.

In order to show the effect of co-annihilations more closely, we draw Fig. 13, where one can see the ΔM dependency on relic density for a specific choice of mixing angle. In the left panel we choose $\sin \theta_d = 0.1$ and that in the right panel for $\sin \theta_d = 0.0001$. The slices with constant ΔM is shown for $\Delta M = \{10, 40, 100, 400\}$ GeV in blue, green, orange, purple lines respectively. We note here, that with larger ΔM , annihilation cross-section increases due to enhancement in Yukawa coupling ($Y \propto \Delta M$ as $\sin \theta_d$ is fixed). However, co-annihilation decreases due to increase in ΔM as $\sigma \propto e^{-\Delta M/M_1}$ specifically for a particular DM mass. Hence the larger is ΔM the smaller is co-annihilation and the larger is the relic density. This is clearly visible in both the panels of Fig. 13. In particular, when $\sin \theta_d$ is small, the effect of co-annihilation is pronounced as contribution from annihilation cross section is less dominant. This is the case shown in the right panel of Fig. 13. Hence the bigger is ΔM , the larger is the required DM mass to satisfy relic density for a given mixing angle $\sin \theta_d$. This is evident from the plot with $\Delta M = 400$ GeV.

For extremely small mixing angle, say $\sin \theta_d = 0.0001$ (shown on the right panel of Fig. 13), the annihilation of $\bar{\psi}_1 \psi_1, \bar{\psi}_1 \psi_2 \rightarrow SM$ particles are highly suppressed. As a result the dominant contribution to relic density arises from $\psi_2 \psi^\pm, \psi^+ \psi^- \rightarrow SM$ particles. This is an interesting consequence of our model. In this case we get a lower limit of the singlet-doublet mixing angle by assuming that the ψ_2, ψ^\pm particles decay to ψ_1 before the latter freezes out from the thermal bath [19]. If the mass splitting between ψ^- and ψ_1 is larger than W^\pm -boson mass, then ψ^- decay preferably occurs through the two body process: $\psi^- \rightarrow \psi_1 + W^-$. However, if the mass splitting between ψ^- and ψ_1 is less than W^\pm boson mass, then ψ^- decays through three body process, say $\psi^- \rightarrow \psi_1 \ell^- \bar{\nu}_\ell$. For the latter case, we get a stronger lower bound on the mixing angle than for two body decay. For the above mentioned channel, the three body decay width of ψ^- is given by [19]:

$$\Gamma = \frac{G_F^2 \sin^2 \theta_d}{24\pi^3} M_2^5 I \quad (4.12)$$

where G_F is the Fermi coupling constant and I is given as:

$$I = \frac{1}{4} \lambda^{1/2} (1, a^2, b^2) F_1(a, b) + 6F_2(a, b) \ln \left(\frac{2a}{1 + a^2 - b^2 - \lambda^{1/2}(1, a^2, b^2)} \right). \quad (4.13)$$

In the above Equation $F_1(a, b)$ and $F_2(a, b)$ are two polynomials of $a = M_1/M_2$ and $b = m_\ell/M_2$, where m_ℓ is the charged lepton mass. Up to $\mathcal{O}(b^2)$, these two polynomials are given by

$$\begin{aligned} F_1(a, b) &= (a^6 - 2a^5 - 7a^4(1 + b^2) + 10a^3(b^2 - 2) + a^2(12b^2 - 7) + (3b^2 - 1)) \\ F_2(a, b) &= (a^5 + a^4 + a^3(1 - 2b^2)). \end{aligned} \quad (4.14)$$

In Eq. (4.13), $\lambda^{1/2} = \sqrt{1 + a^4 + b^4 - 2a^2 - 2b^2 - 2a^2 b^2}$ defines the phase space. In the limit $b = m_\ell/M_2 \rightarrow 1 - a = \Delta M/M_2$, $\lambda^{1/2}$ goes to zero and hence $I \rightarrow 0$. The life time of ψ^- is then given by $\tau \equiv \Gamma^{-1}$. Now to compare the life time of ψ^- with DM freeze out epoch, we assume that the freeze out temperature of DM is $T_f = M_1/20$. Since the DM freezes out during radiation dominated era, the corresponding time of DM freeze-out is given by :

$$t_f = 0.301 g_\star^{-1/2} \frac{m_{\text{pl}}}{T_f^2}, \quad (4.15)$$

where g_\star is the effective massless degrees of freedom at a temperature T_f and m_{pl} is the Planck mass. Demanding that ψ^- should decay before the DM freezes out (i.e. $\tau \lesssim t$) we get

$$\sin\theta_d \gtrsim 1.1789 \times 10^{-5} \left(\frac{1.375 \times 10^{-5}}{I} \right)^{1/2} \left(\frac{200\text{GeV}}{M_2} \right)^{5/2} \left(\frac{g_\star}{106.75} \right)^{1/4} \left(\frac{M_1}{180\text{GeV}} \right). \quad (4.16)$$

Notice that the lower bound on the mixing angle depends on the mass of ψ^- and ψ_1 .

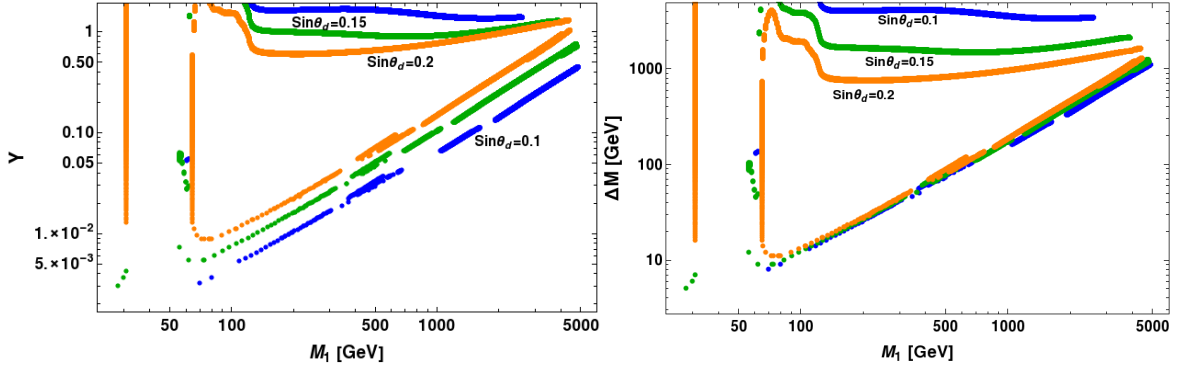


Figure 14. Left: Y versus M_1 (in GeV) for correct relic density (Eq. 4.11). $\sin\theta_d = 0.1, 0.2, 0.15$ (blue, green and orange respectively) has been chosen, while ΔM vary arbitrarily. Right: Same plot in $M_1 - \Delta M$ plane.

In Fig. 14 (left), we plot Y versus M_1 to produce correct relic density with $\sin\theta_d = \{0.1, 0.15, 0.2\}$ (blue, orange, green respectively). In order to be consistent with Eq. (4.4), ΔM has to be adjusted accordingly. It points out a relatively wide DM mass range satisfy the relic density constraint. Main features that emerge out of this figure are as follows: (i) Firstly, there exist a lower DM mass region where Z and H resonances occur. Relic density is easily satisfied in this region for all possible moderate choices of $\sin\theta_d$, independent of Y or ΔM as is seen on the left hand side vertical lines (in both the plots). For large $\sin\theta_d$ this is more prominent as both Z and H mediation is enhanced with larger mixing. (ii) The other point is to note that there are two regions for each $\sin\theta_d$ value which satisfy relic density; one at the below, where Y (on the left) and ΔM (on the right panel) increase with larger DM mass to satisfy relic density. This region is dominantly contributed from co-annihilations as the small Y is not enough to produce annihilations required for relic density. While there is a second region with larger Y (on left) and larger ΔM (on right), more insensitive to DM mass, where relic density is satisfied by appropriate annihilation cross-section, not aided by co-annihilations. Both of these regions (annihilation and co-annihilation domination) meet at some large DM mass ~ 5000 GeV, more clearly visible from the right panel plot. Points above the ‘correct annihilation lines’ (for specific $\sin\theta_d$) provide more than required annihilation and hence those are under abundant regions. Similarly just below those, the annihilation will not be enough to produce correct density and hence are over abundant

regions. Points below the correct co-annihilation regions produce more co-annihilations than required and hence depict under abundant regions.

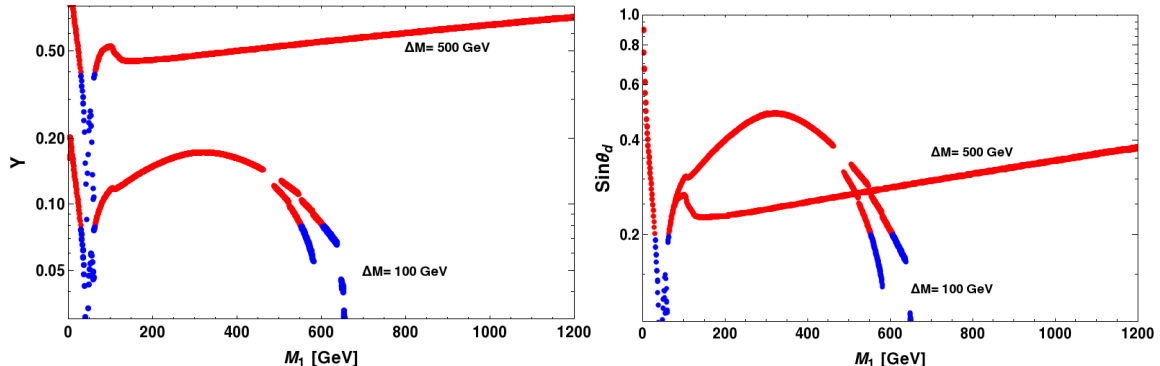


Figure 15. Left: Y versus M_1 (in GeV) for correct relic density (within the range given by Eq. (4.11)) with fixed ΔM at 100, 500 GeV, while $\sin \theta_d$ is allowed to vary. Right: Same plot in $M_1 - \sin \theta_d$ plane. In both panels, blue dots are the allowed points for small $\sin \theta_d$ to satisfy the Y , ΔM abundance via Eq. (4.4).

The other possible correlation in this model for correct relic density can be drawn between DM mass (M_1) and the mixing angle ($\sin \theta_d$) for fixed ΔM . This is shown in Fig. 15 both in $M_1 - Y$ plane (on the left) or in $M_1 - \sin \theta_d$ plane (on the right). For illustration, we choose two widely different values of mass difference: $\Delta M = 100$ GeV and $\Delta M = 500$ GeV. This is clearly understood that with larger ΔM , a larger Y is favored for a specific DM mass in order to satisfy the correct relic abundance. With $\Delta M = 100$ GeV we also note that Y drops substantially around $M_1 \sim 500$ GeV. This is because around this value, co-annihilation process starts contributing and hence it requires a further drop in Y (in terms of mixing angle θ_d) to obtain right relic density which is clearly visible in the right side of Fig. 15 as well. Here we would like to draw the attention that the right relic density line has a split when co-annihilation starts dominating. This is due to the fact that there are two different co-annihilations that occur here with ψ_2 and ψ^\pm . There exist a slight mass difference between these particles and the DM mass is adjusted to either of them to effectively co-annihilate and produce right relic density. For $\Delta M = 500$ GeV, this phenomena of co-annihilation occurs at a very large DM mass and can't be seen from the plot. Resonance drops both in $Y - M_1$ and $\sin \theta_d - M_1$ plots can be observed for $M_1 \sim M_H/2$ and $M_1 \sim M_Z/2$. We also note that beyond $\sin \theta_d \geq 0.2$ as shown by the red points in Fig. 15 break small θ_d limit as has been assumed in Eq. (4.4) and hence discarded within this approximation.

Non-observation of DMs in direct search experiments tend to put a stringent bound on WIMP DM parameter space. Direct search interactions for ψ_1 has two different channels, through Z and H mediation as shown in Fig. 16, where the one through Z mediation dominates over H mediated interaction because of $SU(2)$ gauge coupling. The cross-section

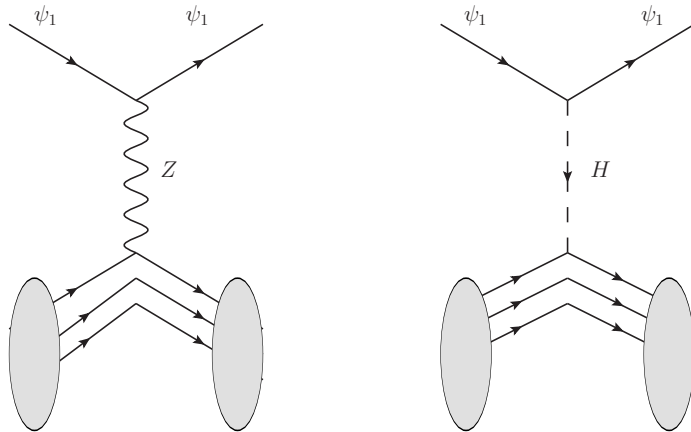


Figure 16. Feynman diagrams for DM to interact with Nucleon.

per nucleon for Z mediation is given by [51, 52]

$$\sigma_{\text{SI}}^Z = \frac{1}{\pi A^2} \mu_r^2 |\mathcal{M}|^2 \quad (4.17)$$

where $\mu_r = M_1 m_n / (M_1 + m_n) \approx m_n$ is the reduced mass, m_n is the mass of nucleon (proton or neutron), A is the mass number of the target nucleus and \mathcal{M} is the amplitude for Z -mediated DM-nucleon cross-section

$$\mathcal{M} = \sqrt{2} G_F [Z(f_p/f_n) + (A - Z)] f_n \sin^2 \theta_d, \quad (4.18)$$

f_p and f_n are the interaction strengths of DM with proton and neutron respectively and Z is the atomic number of the target nucleus. Using $f_n \simeq 1/3$ [53–56], we obtain direct search cross-section per nucleon to be

$$\sigma_{\text{SI}}^Z \simeq 3.75 \times 10^{-39} \text{cm}^2 \sin^4 \theta_d. \quad (4.19)$$

Higgs mediated cross-section depends on can be written as

$$\sigma_{\text{SI}}^h = \frac{1}{\pi A^2} \mu_r^2 [Z f_p + (A - Z) f_n]^2 \quad (4.20)$$

where the effective interaction strengths of DM with proton and neutron are given by:

$$f_{p,n} = \sum_{q=u,d,s} f_{Tq}^{(p,n)} \alpha_q \frac{m_{(p,n)}}{m_q} + \frac{2}{27} f_{TG}^{(p,n)} \sum_{q=c,t,b} \alpha_q \frac{m_{p,n}}{m_q} \quad (4.21)$$

with

$$\alpha_q = \frac{Y \sin 2\theta_d}{M_h^2} \left(\frac{m_q}{v} \right). \quad (4.22)$$

We compute the direct search cross-section with both diagrams using `MicrOmegas` [50]. It turns out that the most stringent constraint on the model and hence on the portal

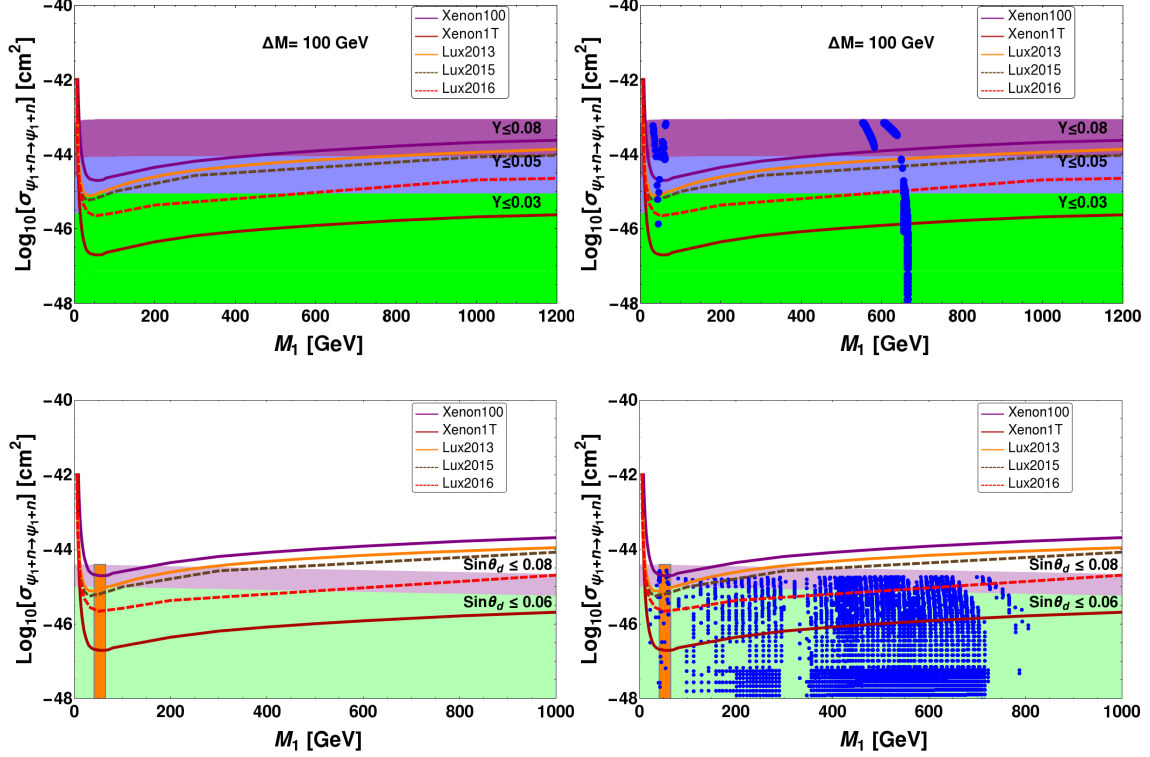


Figure 17. Spin independent direct search cross-section as a function of DM mass. Upper Left Panel: Different Y ranges are indicated $Y : \{0.001 - 0.03\}$ (green), $Y : \{0.03 - 0.05\}$ (blue) and $Y : \{0.05 - 0.08\}$ (purple). $\Delta M = 100$ GeV is used for the scan. Upper Right Panel: Same as left, additional blue dots represent points which satisfy relic density constraint. Lower left panel: Allowed ranges of $\sin \theta_d \leq 0.06, 0.08$ (light green and lilac regions respectively) are shown. Here ΔM varies arbitrarily upto 1.1 TeV. Lower right panel is same as the lower left panel having blue dots representative of points which satisfy relic density constraint. The resonance region is separately indicated in orange. Constraints from Xenon100, Lux 2013, 2015, 2016 data and predictions of Xenon1T are presented.

coupling Y ($\lesssim \sin 2\theta_d \Delta M / (2v)$) comes from the direct search of DM from updated LUX data [57] as demonstrated in Fig. 17. We show the correct region of direct search allowed parameter space in two ways: in upper panel we choose a specific ΔM and vary $\sin \theta_d$ to evaluate spin independent direct search cross-section and show the constraints in terms of Y . On the upper right panel, we also show the relic density allowed points through blue dots for this particular choice of ΔM . In the bottom panel of Fig. 17, instead of choosing a specific ΔM , we vary it arbitrarily upto 1.1 TeV and point out the direct search constraints in terms of mixing angle $\sin \theta_d$. On the right bottom panel, we also show the relic density allowed points through blue dots. Restricting direct search cross-section to experimental limit actually puts a stringent bound on mixing angle $\sin \theta_d$ to tame Z-mediated diagram in particular. We see that the bound from LUX, constraints the coupling: $Y \sim 0.03$ for DM masses $\gtrsim 600$ GeV (green regions in the upper panel of Fig. 17). The Yukawa coupling

needs to be even smaller for small DM mass for example, $M_1 \simeq 200$ GeV. The resonance region is exempted from this constraint for obvious reasons. The annihilation cross-section is enhanced due to s-channel contribution and to tame it to right relic density, one needs much smaller values of mixing angle, which sharply drops the direct search cross-section. Though large couplings are allowed by correct relic density, they are highly disfavored by the direct DM search at terrestrial experiments. From the top right figure, we also see that correct relic density points for a specific ΔM lies in the vicinity of a specific DM mass ~ 700 GeV where co-annihilation plays the crucial role for correct relic density and that doesn't contribute to direct search cross-section at all, so that the blue points yield very small direct search cross-sections. This can easily be extended for other choices of ΔM , where there exist a specific DM mass at which co-annihilation plays a crucial role to yield right relic density, which doesn't contribute to direct search and thus can have very small direct search cross-section as is seen from the right bottom figure. Note also that direct search constraints are less dependent on ΔM as to the mixing angle, which plays otherwise a crucial role in the relic abundance of DM. In bottom panel, we show the parameter space satisfied by relic density constraint for $\sin \theta_d \leq 0.08, 0.06$ (lilac and green regions respectively) to direct search constraints. The direct search tightly constraints the mixing angle to $\sin \theta_d \leq 0.08$, allowing DM masses as heavy as 900 GeV. Tighter constraint in mixing angle, for example, $\sin \theta_d \leq 0.06$, allows smaller DM mass ≥ 500 GeV as can be seen from the cross-over of LUX constraint with relic density allowed parameter space.

In summary, the dark sector phenomenology with the inclusion of vector-like fermions provides a simple extension to SM, with a rich phenomenology with a large region of allowed parameter space from relic density constraints. Direct search on the other hand constrains the mixing to a small value ≤ 0.08 , allowing co-annihilation to play a dominant part to keep the model alive. We will focus on the correlations to non-zero θ_{13} and DM in the following section with the results obtained from above analysis. Note that the $U(1)$ symmetry being global, its spontaneous breaking would lead to potentially dangerous Goldstone boson ($G = \text{Im}\phi$). The problem however can be evaded by gauging the symmetry. Additionally if we assume the corresponding gauge boson to be sufficiently heavy, its existence will not modify our results of the dark matter phenomenology. Another way out is to provide tiny mass to the Goldstone by introducing an explicit symmetry breaking term in the Lagrangian. In this case however the most significant coupling of the Goldstone with Higgs appears through $\lambda_{12}\phi^\dagger\phi H^\dagger H$ coupling. Hence it contributes (considering $m_G \ll m_h/2$) to the invisible decay of the SM Higgs boson [59], $\Gamma_{h \rightarrow G G} \sim \frac{1}{32\pi}[m_h^3/\langle\phi\rangle]\sin^2\alpha$, where α signifies the mixing between the states (H, ϕ) and the physical Higgs fields (h, H') resulting (H' is the heavy Higgs) from non-zero λ_{12} . In the limit of λ_{12} to zero, α vanishes. Using the present limit on the branching ratio of Higgs invisible decay [60, 61], the coupling λ_{12} (involved in the definition of mixing angle α) is expected to be small ($\ll 1$). If we assume a very small value of λ_{12} , $\sim 10^{-8}$ or even smaller, then it can be shown that the Goldstone can never be in thermal equilibrium [62] and hence they can not contribute to the primordial abundance through freeze out mechanism ³ and we may basically ignore its presence for our purpose.

³In this case, the other option could be [63] the freeze-in mechanism [64]. It requires a detailed study and is at present beyond the scope of current analysis.

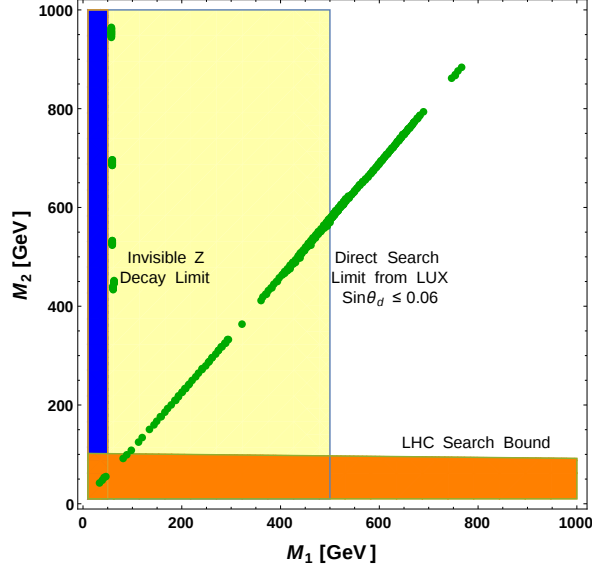


Figure 18. Summary of all constraints in $M_1 - M_2$ parameter space from relic density with $\sin \theta_d = 0.06$ (green dots), direct search (Yellow region is forbidden by updated LUX with $\sin \theta_d \sim 0.06$), invisible Z-decay (blue region is forbidden) and collider (LHC) search limit (orange region is disallowed with an over estimation for $\sin \theta_d = 0.1$).

We can now put together all the constraints for a specific choice of $\sin \theta_d = 0.06$ into the plane of $M_1 - M_2$ to show the allowed parameter space of the model. This is what we have done in Fig. 18 following

$$\begin{aligned}
 \text{Inv Z decay} &: M_1 < \frac{M_z}{2} \sim 45 \text{ GeV} \rightarrow \sin \theta_d \lesssim 0.00125 \\
 \text{Inv H decay} &: M_1 < \frac{M_h}{2} \sim 63 \text{ GeV} \rightarrow \sin \theta_d \lesssim 0.1 \\
 \text{Relic Density} &: M_2 \lesssim M_1 + 100 \text{ GeV for } \sin \theta_d \lesssim 0.1 \\
 \text{Direct Search} &: M_1 \geq 500 \text{ GeV for } \sin \theta_d \sim 0.06 \\
 \text{Collider Bound} &: M_2 \simeq M^\pm \geq 101 \text{ GeV for } \sin \theta_d \sim 0.06.
 \end{aligned}$$

We choose $\sin \theta_d = 0.06$ as a reference value as it satisfies all of the constraints discussed here. We see that a sizable part of the DM parameter space is allowed shown by the green dotted points, excepting for the direct search bound shown by yellow band, a blue band disfavored by the Invisible Z decay and orange band disfavored by direct collider search data [58]. One should also note here that if we choose a smaller $\sin \theta_d$ to illustrate the case, a larger DM mass region is allowed by direct search constraint. Green dotted points show relic density allowed regions of the model in $M_1 - M_2$ plane. We note here that for $\sin \theta_d < 0.1$, only co-annihilation can provide with right relic density, hence is independent of the choices $\sin \theta_d \sim 0.1$ or ~ 0.06 as has been chosen in Fig. 18.

5 Correlation between Dark and Neutrino Sectors

As stated before, our description of the DM sector is composed of a vector like $SU(2)_L$ doublet and a neutral singlet fermions which interact with the SM sector via Eq. (2.8). We have seen in the previous section the importance of the effective coupling Y in determining the mixing between the singlet and doublet components of DM (see Eq. (4.4)). This mixing in turn plays the crucial role in realizing the correct relic density as well as involved in the direct search cross section (see Eqs. (4.7) and (4.17, 4.20)). Note that this effective coupling Y is generated from the vev of the flavon ϕ through $Y = \epsilon^n$, where the n is the unknown $U(1)$ charge assigned to ϕ . However this vev alone does not appear separately in our dark matter analysis. On the other hand, we have noted earlier the involvement of ϵ parameter in the neutrino phenomenology, in particular in producing θ_{13} in the correct ballpark. So we observe that the allowed value of nonzero θ_{13} and the Higgs portal coupling of a vector like dark matter can indeed be obtainable from a $U(1)$ flavor extension of the SM. In this section we aim to fix the charge n from combining the results of neutrino as well as the dark matter analyses. This complementarity between the neutrino and the DM sector will be clear as we proceed below in summarizing constraints on ϵ and Y obtained from neutrino and DM analyses respectively.

Section 3 was devoted to neutrino phenomenology, where we have discussed four different cases. In case A, we find that the parameter ϵ is clearly determined to be within the range $0.328 - 0.413$ in order to keep $\sin\theta_{13}$ in agreement with experimental data (see Fig. 1). In cases B and C however, this correlation between ϵ and θ_{13} is not that transparent as it depends also on the CP phase δ . Combining all the phenomenological constraints (*e.g.* on $\sum_i m_{\nu_i}$), we have provided the range of ϵ in Table 3 and 4 for cases B and C respectively. The range of ϵ corresponding to case D is similar to case A. On the other hand, the information on Y is embedded in the relic density and direct detection cross section.

In the left upper panel of Fig. 17, we plot the direct search cross-section against dark matter mass M_1 for a fixed choice of $\Delta M = 100$ GeV. In this plot, we indicate regions allowed by direct search experimental limits. Since each point in the region allowed by direct search correspond to a specific relic density, once we incorporate both the relic density and direct search limit by LUX 2016, we find the allowed region is narrowed down as shown in the right upper panel of Fig. 17 (indicated by blue patch).

Similarly the left lower panel (left and right) of Fig. 17 shows the allowed (by both relic density and LUX 2016) region of parameter space where variation of M_2 is restricted up to 1.1 TeV with $\sin\theta_d \leq 0.2$. We find that an upper limit on $\sin\theta_d$ is prevailing from this plot. Combining relic density constraint and direct search limits, we find the allowed region indicated by blue dots in the right lower panel of Fig. 17. In order to obtain limits on Y while ΔM and $\sin\theta_d$ are varied, we have provided a scatter plot of Y versus M_1 in Fig. 19. In producing this plot, we have varied M_2 (up to 1.1 TeV), $10^{-7} < \sin\theta_d < 0.2$. Here red dots correspond to those points which are disallowed by LUX 2016 even if these satisfy the relic density constraint. The blue patch indicates the region allowed by both the relic density and LUX 2016 data having $\Delta M > m_W$. For $\Delta M < m_W$, we use a lower limit on $\sin\theta_d$ obtained from Eq. (4.16). Hence the points in magenta satisfy the above $\sin\theta_d$

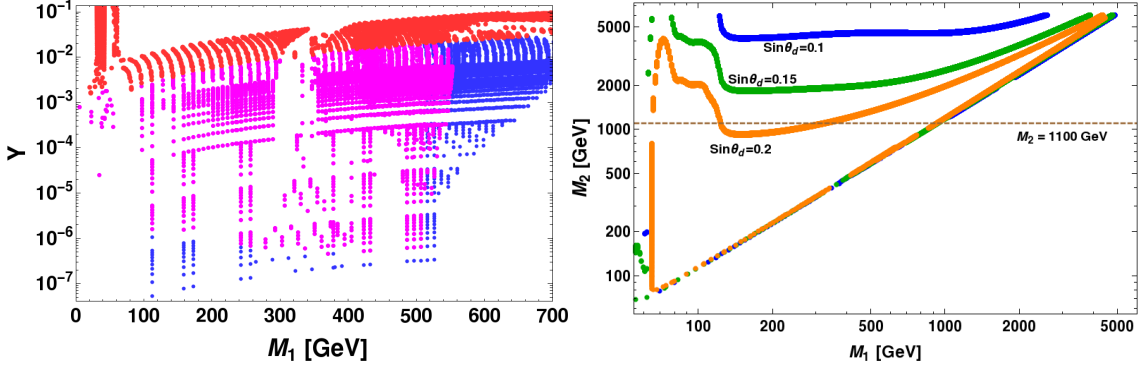


Figure 19. Left Panel: Y vs M_1 scatter plot for correct relic density (Eq. 4.11). Here $\sin\theta_d$ (10^{-6} -0.2) and ΔM (1-1100 GeV) varies simultaneously. The top red points are disallowed by Lux 2016 direct search constraint. Both magenta and blue dots simultaneously satisfies relic density and Lux 2016 direct search constraints. The magenta dots additionally satisfies the condition $\Delta M < M_W$. Right Panel: M_1 versus M_2 (in GeV) for correct relic density. $\sin\theta_d = 0.1, 0.2, 0.15$ (blue, green and orange respectively) has been chosen, while ΔM varies. The left panel is consistent with this plot upto $M_2 = 1.1$ TeV as marked by the horizontal dashed line in this plot.

constraint and represent the allowed region by relic density and direct search limits. From this plot we can clearly see the upper limit of Y is almost 0.03 while the lower limit of it can be very small, $\sim 10^{-7}$. Note that the Y region limited by the choice of upper value of $M_2 = 1.1$ TeV is consistent with our earlier plot in Fig. 14 with fixed $\sin\theta_d$ values. For elaboration purpose, we provide the figure in the right panel of Fig. 19, which is the same plot as Fig. 14 except that it is now plotted in terms of M_2 vs. M_1 . The narrow patch for a fixed $\sin\theta_d$ becomes wider as we varied $\sin\theta_d$ as well. The horizontal dashed line indicates our consideration of keeping the variation of M_2 within 1.1 TeV.

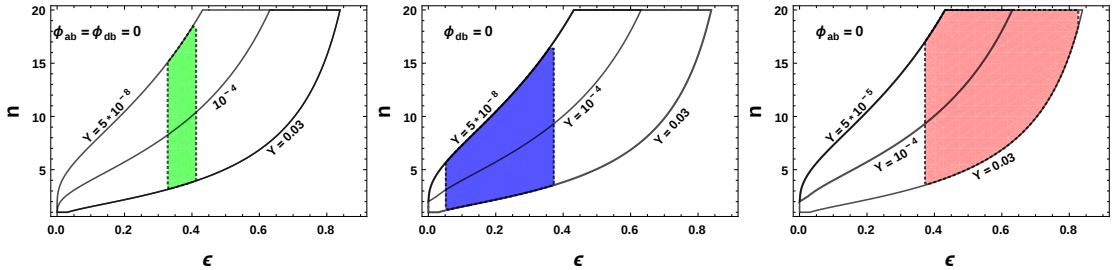


Figure 20. n vs ϵ to generate different values of $Y = \epsilon^n$ for (a) $\phi_{db} = \phi_{ab} = 0$ (left), (b) $\phi_{db} = 0$ (middle) and (c) $\phi_{ab} = 0$ (right).

We summarize here these constraints on ϵ and $Y = \epsilon^n$ to determine the unknown flavor charge n of the dark matter in our scenario. It is shown in Fig. 20. Colored patch in each plot corresponds to the allowed range of ϵ obtained in section 3 for Cases A(D), B

and C. In the left-most panel of Fig. 20, we have shown the allowed values of n where the CP-violating phases are taken to be zero corresponding to Case A. As the direct search of DM restricts the Y values to be $Y \lesssim 0.03$, we get $n \gtrsim 2$. Different contour lines with different Y values are shown in the figure. A similar conclusion holds for the other case (Case D) with $\phi_{db} = \phi_{ab} = \beta$. On the other hand, if $\phi_{ab} \neq \phi_{db}$ then a larger range of n values are expected to be allowed. In particular, by setting $\phi_{db} = 0$ and $\phi_{ab} \neq 0$ (as shown in middle panel of Fig. 20) we see that lower limit on n starts from 1. On the other hand, if $\phi_{ab} = 0$ and $\phi_{db} \neq 0$ (as shown in the right panel of Fig. 20) then n can take values starting from 3. Thus we conclude that the non-zero values of phases introduce more uncertainty in specifying n . The future measurements of Dirac CP phase δ and a more stringent constraints from Direct search experiments would reduce this uncertainty in n .

6 Conclusions

In this paper we have explored a $U(1)$ flavor extension of the SM in order to establish a possible correlation between the SM sector (more specifically neutrino sector) and the DM one, in particular between the reactor lepton mixing angle $\sin\theta_{13}$ and the interaction of dark matter with SM Higgs. To start with, we have considered a tri-bimaximal mixing pattern (*i.e.* with $\theta_{13} = 0$) for the lepton mixing matrix originated from a typical flavor structure of the neutrino mass matrix guided by the non-Abelian flavor symmetry, where the charged lepton mass matrix is found to be diagonal. In its simplest version, we achieve the TBM structure of the neutrino mass matrix by assuming an $A_4 \times Z_3$ symmetry where the effective dimension six operators involving A_4 flavons contributes to Majorana masses for light neutrinos. The symmetry forbids the usual dimension five operator. On the other hand, the dark sector consists of two vector-like fermions, one is a $SU(2)_L$ doublet and the other one is a SM gauge singlet. In addition we assume the existence of a $U(1)$ flavor symmetry under which the DM fields as well as two flavons, ϕ and η , are charged. It is interesting to note that with the vector-like fermions present in the dark sector, there exists a replica of SM Yukawa interaction in the dark sector which involves flavon ϕ . The $U(1)$ symmetry of the model was broken at a high scale by the vev of that flavon field ϕ to a remnant Z_2 under which the dark sector particles are odd. As a result the lightest odd particles becomes a viable candidate of dark matter. Moreover, a higher dimensional operator involving ϕ and η constitutes a correction to the TBM pattern of the neutrino mass matrix which leads to a non-zero value of $\sin\theta_{13}$. The involvement of ϕ ensures that $B - L$ breaking vev is also involved in this correction term. As a result we are able to show that the non-zero value of $\sin\theta_{13}$ is proportional to the Higgs portal coupling, $Y = (\phi/\Lambda)^n \equiv \epsilon^n$, of the dark matter which gives rise to correct relic density measured by WMAP and PLANCK and consistent with direct DM search bound from LUX. Finally it is interesting to note that Y , on one hand is related to the mixing in the neutrino sector, while it also crucially controlled by the mixing involved in the dark sector. We also find that the current allowed values of $\sin\theta_{13}$ indicates the $U(1)$ charge of DM $\gtrsim 1$ which can be probed at the future direct DM search experiments such as Xenon-1T. The next to lightest stable

particle (NLSP) is a charged fermion which can be searched at the LHC [22, 23]. In the limit of small $\sin\theta_d$, the NLSP can give rise to a displaced vertex at LHC, a rather unique signature of the model discussed in ref. [19]. We argue that this is a minimal extension to SM to accommodate DM and non-zero $\sin\theta_{13}$ by using a flavor symmetric approach.

Acknowledgments

The work of SB is partially supported by DST INSPIRE grant no PHY/P/SUB/01 at IIT Guwahati. NS is partially supported by the Department of Science and Technology, Govt. of India under the financial Grant SR/FTP/PS-209/2011.

References

- [1] S. Fukuda *et al.* [Super-Kamiokande Collaboration], Phys. Lett. B **539**, 179 (2002) [hep-ex/0205075].
- [2] Y. Ashie *et al.* [Super-Kamiokande Collaboration], Phys. Rev. D **71**, 112005 (2005) [hep-ex/0501064].
- [3] P. Adamson *et al.* [MINOS Collaboration], Phys. Rev. Lett. **106**, 181801 (2011) [arXiv:1103.0340 [hep-ex]].
- [4] T. Araki *et al.* [KamLAND Collaboration], Phys. Rev. Lett. **94**, 081801 (2005) [hep-ex/0406035].
- [5] G. Hinshaw *et al.* [WMAP Collaboration], Astrophys. J. Suppl. **208**, 19 (2013) [arXiv:1212.5226 [astro-ph.CO]].
- [6] P. A. R. Ade *et al.* Planck Collaboration, Astron. Astrophys. **571**, A16 (2014), arXiv:1303.5076 [astro-ph.CO].
- [7] P. A. R. Ade *et al.* [Planck Collaboration], Astron. Astrophys. **594**, A13 (2016) doi:10.1051/0004-6361/201525830 [arXiv:1502.01589 [astro-ph.CO]].
- [8] G. Bertone, D. Hooper and J. Silk, Phys. Rept. **405**, 279 (2005), arXiv:hep-ph/0404175.
- [9] C. D. Froggatt and H. B. Nielsen, Nucl. Phys. B **147**, 277 (1979).
- [10] E. Ma and G. Rajasekaran, Phys. Rev. D **64** (2001) 113012 [hep-ph/0106291].
- [11] G. Altarelli and F. Feruglio, Nucl. Phys. B **741**, 215 (2006) [hep-ph/0512103].
- [12] F. Capozzi, G. L. Fogli, E. Lisi, A. Marrone, D. Montanino and A. Palazzo, Phys. Rev. D **89**, no. 9, 093018 (2014) [arXiv:1312.2878 [hep-ph]].
- [13] M. C. Gonzalez-Garcia, M. Maltoni and T. Schwetz, JHEP **1411**, 052 (2014) [arXiv:1409.5439 [hep-ph]].
- [14] D. V. Forero, M. Tortola and J. W. F. Valle, Phys. Rev. D **90**, no. 9, 093006 (2014) [arXiv:1405.7540 [hep-ph]].
- [15] Y. Abe *et al.* [Double Chooz Collaboration], Phys. Rev. Lett. **108**, 131801 (2012) [arXiv:1112.6353 [hep-ex]].
- [16] F. P. An *et al.* [Daya Bay Collaboration], Phys. Rev. Lett. **108**, 171803 (2012) [arXiv:1203.1669 [hep-ex]].

- [17] J. K. Ahn *et al.* [RENO Collaboration], Phys. Rev. Lett. **108**, 191802 (2012) [arXiv:1204.0626 [hep-ex]].
- [18] K. Abe *et al.* [T2K Collaboration], Phys. Rev. Lett. **112**, 061802 (2014) [arXiv:1311.4750 [hep-ex]].
- [19] S. Bhattacharya, N. Sahoo and N. Sahu, Phys. Rev. D **93**, no. 11, 115040 (2016) [arXiv:1510.02760 [hep-ph]].
- [20] S. Bhattacharya, B. Karmakar, N. Sahu and A. Sil, Phys. Rev. D **93**, no. 11, 115041 (2016) [arXiv:1603.04776 [hep-ph]].
- [21] E. Aprile *et al.* [XENON Collaboration], [arXiv:1512.07501 [physics.ins-det]].
- [22] C. Arina, R. N. Mohapatra and N. Sahu, Phys. Lett. B **720** (2013) 130 [arXiv:1211.0435 [hep-ph]].
- [23] C. Arina, J. O. Gong and N. Sahu, Nucl. Phys. B **865**, 430 (2012) [arXiv:1206.0009 [hep-ph]].
- [24] S. F. King and C. Luhn, JHEP **1109**, 042 (2011) [arXiv:1107.5332 [hep-ph]].
- [25] M. Holthausen, M. Lindner and M. A. Schmidt, Phys. Rev. D **87**, no. 3, 033006 (2013) [arXiv:1211.5143 [hep-ph]].
- [26] L. Dorame, S. Morisi, E. Peinado, J. W. F. Valle and A. D. Rojas, Phys. Rev. D **86**, 056001 (2012) [arXiv:1203.0155 [hep-ph]].
- [27] P. F. Harrison, D. H. Perkins and W. G. Scott, Phys. Lett. B **458**, 79 (1999) [hep-ph/9904297].
- [28] B. Karmakar and A. Sil, Phys. Rev. D **91**, 013004 (2015) [arXiv:1407.5826 [hep-ph]].
- [29] G. C. Branco, R. Gonzalez Felipe, F. R. Joaquim and H. Serodio, Phys. Rev. D **86**, 076008 (2012) [arXiv:1203.2646 [hep-ph]].
- [30] B. Karmakar and A. Sil, Phys. Rev. D **93**, no. 1, 013006 (2016) [arXiv:1509.07090 [hep-ph]].
- [31] B. Karmakar and A. Sil, arXiv:1610.01909 [hep-ph].
- [32] Y. Shimizu, M. Tanimoto and A. Watanabe, Prog. Theor. Phys. **126**, 81 (2011) [arXiv:1105.2929 [hep-ph]].
- [33] L. Calibbi, A. Crivellin and B. Zaldivar, Phys. Rev. D **92**, no. 1, 016004 (2015) [arXiv:1501.07268 [hep-ph]].
- [34] M. Hirsch, S. Morisi, E. Peinado and J. W. F. Valle, Phys. Rev. D **82**, 116003 (2010) [arXiv:1007.0871 [hep-ph]].
- [35] M. S. Boucenna, M. Hirsch, S. Morisi, E. Peinado, M. Taoso and J. W. F. Valle, JHEP **1105**, 037 (2011) [arXiv:1101.2874 [hep-ph]].
- [36] R. de Adelhart Toorop, F. Bazzocchi and S. Morisi, Nucl. Phys. B **856**, 670 (2012) [arXiv:1104.5676 [hep-ph]].
- [37] Y. Hamada, T. Kobayashi, A. Ogasahara, Y. Omura, F. Takayama and D. Yasuhara, JHEP **1410**, 183 (2014) [arXiv:1405.3592 [hep-ph]].
- [38] W. C. Huang, JHEP **1411**, 083 (2014) [arXiv:1405.5886 [hep-ph]].
- [39] M. Lattanzi, R. A. Lineros and M. Taoso, New J. Phys. **16**, no. 12, 125012 (2014) [arXiv:1406.0004 [hep-ph]].

- [40] I. de Medeiros Varzielas, O. Fischer and V. Maurer, *JHEP* **1508**, 080 (2015) [arXiv:1504.03955 [hep-ph]].
- [41] E. Ma, *Phys. Lett. B* **754**, 114 (2016) [arXiv:1506.06658 [hep-ph]].
- [42] I. Medeiros Varzielas and O. Fischer, *JHEP* **1601**, 160 (2016) [arXiv:1512.00869 [hep-ph]].
- [43] A. Mukherjee and M. K. Das, *Nucl. Phys. B* **913**, 643 (2016) [arXiv:1512.02384 [hep-ph]].
- [44] J. M. Lamprea and E. Peinado, arXiv:1603.02190 [hep-ph].
- [45] G. Altarelli and F. Feruglio, *Rev. Mod. Phys.* **82**, 2701 (2010) [arXiv:1002.0211 [hep-ph]].
- [46] K. Griest and D. Seckel, *Phys. Rev. D* **43**, 3191 (1991); A. Chatterjee and N. Sahu, *Phys. Rev. D* **90**, no. 9, 095021 (2014) [arXiv:1407.3030 [hep-ph]].
- [47] G. Cynolter and E. Lendvai, *Eur. Phys. J. C* **58**, 463 (2008) [arXiv:0804.4080 [hep-ph]].
- [48] T. Cohen, J. Kearney, A. Pierce and D. Tucker-Smith, *Phys. Rev. D* **85**, 075003 (2012) [arXiv:1109.2604 [hep-ph]].
- [49] C. Cheung and D. Sanford, *JCAP* **1402**, 011 (2014) [arXiv:1311.5896 [hep-ph]].
- [50] G. Belanger, F. Boudjema, A. Pukhov and A. Semenov, *Comput. Phys. Commun.* **180**, 747 (2009) [arXiv:0803.2360 [hep-ph]].
- [51] M. W. Goodman and E. Witten, *Phys. Rev. D* **31**, 3059 (1985).
- [52] R. Essig, *Phys. Rev. D* **78**, 015004 (2008) [arXiv:0710.1668 [hep-ph]].
- [53] R. Koch, *Z. Phys. C* **15**, 161 (1982),
- [54] J. Gasser, H. Leutwyler and M. E. Sainio, *Phys. Lett. B* **253**, 260 (1991).
- [55] M. M. Pavan, I. I. Strakovsky, R. L. Workman and R. A. Arndt, *PiN Newslett.* **16**, 110 (2002) [hep-ph/0111066].
- [56] A. Bottino, F. Donato, N. Fornengo and S. Scopel, *Phys. Rev. D* **78**, 083520 (2008) [arXiv:0806.4099 [hep-ph]].
- [57] D. S. Akerib *et al.*, arXiv:1608.07648 [astro-ph.CO].
- [58] K. A. Olive *et al.* [Particle Data Group Collaboration], *Chin. Phys. C* **38**, 090001 (2014).
- [59] A. S. Joshipura and J. W. F. Valle, *Nucl. Phys. B* **397**, 105 (1993).
- [60] G. Aad *et al.* [ATLAS Collaboration], *JHEP* **1601**, 172 (2016) doi:10.1007/JHEP01(2016)172 [arXiv:1508.07869 [hep-ex]].
- [61] V. Khachatryan *et al.* [CMS Collaboration], *JHEP* **1702**, 135 (2017) doi:10.1007/JHEP02(2017)135 [arXiv:1610.09218 [hep-ex]].
- [62] C. P. Burgess, M. Pospelov and T. ter Veldhuis, *Nucl. Phys. B* **619**, 709 (2001) doi:10.1016/S0550-3213(01)00513-2 [hep-ph/0011335].
- [63] M. Frigerio, T. Hambye and E. Masso, *Phys. Rev. X* **1**, 021026 (2011) doi:10.1103/PhysRevX.1.021026 [arXiv:1107.4564 [hep-ph]].
- [64] L. J. Hall, K. Jedamzik, J. March-Russell and S. M. West, *JHEP* **1003**, 080 (2010) doi:10.1007/JHEP03(2010)080 [arXiv:0911.1120 [hep-ph]].